Origin of discordant U Pb dates in non-metamict zircons in intrusives deformed at granulite facies: Grain scale processes, and relevance to Cambrian orogeny, Eastern Ghats Belt, India

Anwesa Banerjee, Sandra Piazolo, Nathan Cogne, Abhijit Bhattacharya, N. Prabhakar

Journal Pre-proof

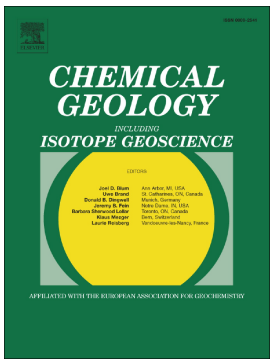

Origin of discordant U-Pb dates in non-metamict zircons in intrusives deformed at granulite facies: Grain scale processes, and relevance to Cambrian orogeny, Eastern Ghats Belt, India

Anwesa Banerjee, Sandra Piazolo, Nathan Cogne, Abhijit Bhattacharya, N. Prabhakar

PII: S0009-2541(24)00326-7

DOI: https://doi.org/10.1016/j.chemgeo.2024.122246

Reference: CHEMGE 122246

To appear in: *Chemical Geology*

Received date: 13 February 2024

Revised date: 1 June 2024

Accepted date: 20 June 2024

Please cite this article as: A. Banerjee, S. Piazolo, N. Cogne, et al., Origin of discordant U-Pb dates in non-metamict zircons in intrusives deformed at granulite facies: Grain scale processes, and relevance to Cambrian orogeny, Eastern Ghats Belt, India, *Chemical Geology* (2023), https://doi.org/10.1016/j.chemgeo.2024.122246

Origin of discordant U-Pb dates in non-metamict zircons in intrusives deformed at granulite facies: Grain scale processes, and relevance to Cambrian orogeny, Eastern Ghats Belt, India

Anwesa Banerjee[1*], Sandra Piazolo[2], Nathan Cogne[3], Abhijit Bhattacharya[4], N Prabhakar[1]

[1] Department of Earth Sciences, Indian Institute of Technology Bombay, Powai, Mumbai 400 076, India

[2]Scool of Earth and Environmental Sciences, Priestly Building, Room 7.13, University of Leeds, LS2 9JT, United Kingdom

[3]Plateforme GeOHeLiS, Géosciences Rennes UMR 6118, Université Rennes 1, 35042 Rennes Cedex, France

[4]180B Hijli Co-operative Society, Kharagpur 721 306, West Bengal, India

Corresponding author (*)

email ID: anwesabanerjee91@gmail.com

phone No: +91 99323 89411

Highlights (85 characters including spaces)

1. Complex chemical zoning and structures in zircons in high-T granitoid-ferrodiorite **[85]**
2. Identical U-Pb discordia in multiple samples; intercepts at ~980 Ma and ~495 Ma **[82]**
3. 980 Ma: age of oscillatory zoned in Y, Hf, U zircon xenocrysts in 495 Ma intrusive **[85]**
4. 495 Ma: melt-mediated xenocryst embayment, zone truncation, epitaxial mantle growth **[86]**
5. Melt-mediated variable isotope inheritance led to discordant dates **[70]**

ABSTRACT (368 words)

Interpreting the origin of U-Pb discordance in zircons in intrusives that experience high-T metamorphic-deformation events is challenging. We investigate in depth the origin of U-Pb dates obtained from garnet-bearing border zone granitoids and a sheared ferrodiorite dyke bordering the Balangir anorthosite pluton, eastern India. The crustal domain is known for discordant ages resulting in disputes regarding the age of intrusion and multiple granulite facies events. We shed light on the origin of the discordant dates utilizing CL imaging, electron backscatter diffraction analysis, trace element mapping in zircons, and Ti-in-zircon thermometry.

Zircons in the foliated border zone granitoids (BZG) comprise (a) embayed cores with varying Y, U and Hf oscillatory zones, and (b) well-faceted chemically-homogeneous mantles crystallographically continuous with the cores, which truncate the oscillatory zones. In the intensely sheared ferrodiorite, cauliflower-shaped zircons possess profuse micropores and micro-fractures. Ti-in-zircon temperatures (700–950 °C) overlap in the texturally-distinct zircons, but are somewhat lower in the mantles/cauliflower-shaped zircons relative to the oscillatory-zoned cores in BZGs.

LA-ICP-MS dates of zircons in four samples constitute a near-unique discordia line with the upper and lower intercepts at ca. 980 Ma and 495 Ma. Interestingly, dates from the mantles are highly variable with no correlation between age decrease and distance to the cores. The lack of concordant dates at the two intercepts, and the increase in discordance away from the intercepts preclude episodic zircon growth, and suggests a single-stage granulite facies event (ca. 495 Ma) that modified the ~980 Ma zircon xenocrysts entrained from protoliths into the intrusives. We propose the age discordance was caused by melt-mediated high-T interface coupled dissolution-precipitation processes at ~495 Ma. Variable inheritance of isotopic signatures of ~980 Ma zircon xenocrysts in the younger zircons contributed to discordance in U-Pb systematics; the effect of variable inheritance of ~ 980 Ma isotope signatures is less pronounced in the cauliflower-shaped zircons crystallized at ~480 Ma from HFSE enriched ferrodiorite residual from high degree of plagioclase fractionation.

Our results are consistent with a distinct Cambrian (~495 Ma) orogeny involving emplacement of anorthosite pluton and related intrusives and high-T granulite-facies deformation-metamorphism in the ~980 Ma Eastern Ghats Province, and are a direct record of Cambrian collision between the Eastern Ghats Province and the Archean cratonic nucleus.

Keywords: Zircon U-Pb dating; fluid-assisted epitaxial zircon growth; age inheritance; Cambrian vs. Rodinia collision; Eastern Ghats Belt; Rayner Complex, Antarctica

1. INTRODUCTION

Zircon ($ZrSiO_4$) is perhaps the most used mineral to determine robust dates in rocks. However, assigning these dates to ages of geologic events is complex. Diverse processes are suggested to modify older dates by younger processes, e.g., intra-crystalline diffusion (Connelly, 2001); radiation damage (Cherniak et al., 1991; Nasdala et al., 1998; Meldrum et al., 1998), high-T metamorphism (McFarlane et. al., 2005; Flowers et al., 2010), crystal plastic deformation both through recrystallization (Pidgeon, 1992; Vonlanthen et al., 2012; Piazolo et al., 2012, Corvò et al., 2023) and fast pipe diffusion along dislocation arrays (Piazolo et al. 2016), and/or incorporation and redistribution of trace elements (Piazolo et al. 2016, Kunz et al., 2018; Huijsmans et al. 2022), existence of nanoscale Pb reservoirs (Peterman et al., 2016), grain fracturing (Rimsa et al., 2007; Tretiakova et al., 2016) and deformation-driven and fluid-mediated dissolution-reprecipitation (Wayne and Sinha, 1988; Timms et al., 2006; Langone et al., 2017, Bogdanova et al. 2021, Corvò et al., 2023, Fougerouse et al., 2024).

Analogue experiments provide crucial inputs in understanding processes that modify the internal structures and re-distribute elements vis-à-vis isotope ratios in zircon. Based on KBr crystals reacting with a saturated solution of KCl in H_2O, Spruzeniece et al. (2017) suggest that the reaction products inherit the crystallographic orientations of the reactant phases, even if it has been previously deformed. In the latter case, replaced materials do exhibit sub-grains and lattice distortions similar to the deformation microstructures; however, in the replaced areas, distortions are less well organized than in the initially deformed grains. Varga et al. (2020) suggests neo-crystallized monazites partly inherit the age of the precursor grains, and results in dispersion of the ages in precursor monazites, and thus the isotope ratios may not faithfully record the exact age of the newly precipitated monazite.

The difficulty in assigning U-Pb zircon dates to the age of geologic event is especially complex in rocks that record multiple high-T events close to and/or exceeding the closure temperature of intra-crystalline diffusion in zircon (at T ~ 900 °C; Lee et al., 1997; Braun et al., 2006; Cherniak and Watson, 2001, 2003). Such complexity arises because high-T promotes diffusion (Cherniak and Watson, 2001), and deformation strain induces imperfections that enhance grain boundary as well as intra-crystalline diffusion in zircons (Timms et al., 2006; Moser et al., 2009; Peterman et al., 2016). Additionally, melts (and/or fluids) may promote dissolution of older zircons (cf. Harrison and Watson, 1983; Harrison et

al., 2007) and re-precipitation of younger zircons or zircon mantles due to changes in the physicochemical conditions (e.g., Fougerouse et al. 2024). These processes either in tandem or in isolation may obliterate/modify the original isotopic ratios.

The border zone granitoids (BZG) and ferrodiorites, which border the Balangir anorthosite pluton close to the NW margin of the Eastern Ghats Province, Eastern India (Bhattacharya et al.,1988) (Fig. 1a-c), were deformed and metamorphosed at granulite facies conditions. Zircons from these rocks have previously been shown to show widespread, largely unexplained discordances (Krausse et al. 2001). To investigate the underlying processes responsible for the discordance and interpret their U-Pb dates obtained by LA-ICP-MS, we adopt a multidisciplinary approach involving analyses of internal structures and external morphologies of the zircon grains (Pidgeon, 1992; Hanchar and Miller, 1993; Corfu et al., 2003; Gagnevin et al., 2010), quantitative crystallographic orientation analysis, Ti-in-zircon thermometry and existing mineral thermo-barometry, and micron-scale variations of element abundances in the zircon grains (Pidgeon, 1992; McFarlane et al., 2005; Flowers et al., 2010; Langone et al., 2017; Kunz et al., 2018; Ge et al., 2019). At the regional scale, the results have important bearing on constraining two temporally distinct high-T events, and their relevance to the time of collision between the Eastern Ghats Province and the Indian landmass, e.g., the early Neoproterozoic (Rodinia) versus Cambrian (Gondwanaland) collision (Nasipuri et al., 2018).

1. GEOLOGICAL BACKGROUND

In the Eastern Ghats Belt, the Eastern Ghats Province EGP (Fig. 1a; Rickers et al., 2001) is composed of 1.1–0.9 Ga (Aftallion et al., 1988; Raith et al., 2014; Mitchell et al., 2019) ultra high-T granulite facies gneisses (Nasipuri et al., 2008; Padmaja et al., 2022), foliated garnet-bearing charnockite-enderbite-granite intrusives (Mukherjee and Bhattacharya, 1997), massif anorthosite (Fig. 1a) and nepheline syenite complexes. The Balangir anorthosite massif (Tak et al., 1966; Mukherjee et al., 1986 Mukherjee, 1989; Dobmeier, 2006; Nasipuri and Bhadra, 2013; Fig. 1b, c) is located ~20 km SE of the WNW margin of the EGP, tectonically juxtaposed with the >2.5 Ga lithodemic units of the Bastar Craton (Biswal and Sinha, 2003; Gupta et al., 2000; Biswal et al., 2004; Bhadra et al., 2007; Nasipuri et al., 2018). The Balangir anorthosite complex intrudes into the poly-deformed ultra-high T anatectic gneisses. It is dominated by anorthosite *sensu stricto* and leuconorite (orthopyroxene > clinopyroxene). The pluton is mantled by a suite of garnet-bearing mangerite, charnockite and granite,

collectively termed as the bordering zone granitoids, BZG (Raith et al., 1997; Bhattacharya et al., 1998; Fig. 1c).

The BZGs (Fig. 2a) and the anorthosites (Fig. 2b) at the pluton margin are characterized by a single penetrative tectonic foliation that mimics the margin of the massif (Nasipuri and Bhattacharya, 2007; Nasipuri et al., 2011). The intensity of margin-parallel foliation (MPF) weakens radially outward from the granitoid-anorthosite interface (Nasipuri and Bhattacharya, 2007). Within the anorthosite pluton, igneous features such as trains of euhedral plagioclase grains described by Nasipuri and Bhattacharya (2007) are rare. Strongly-embayed un-recrystallized gray-coloured xenomorphic grains of relict plagioclase phenocrysts in a sugary white mosaic of recrystallized plagioclase are the only evidence of the igneous ancestry of the rocks (Nasipuri and Bhattacharya, 2007).

Sandwiched between the anorthosite massif and the high-K BZGs, a suite of low-K, Si ferrodiorites (Fig. 3a-d) with high abundances of plagioclase-incompatible high field strength elements (Zr, Hf, REEs; Bhattacharya et al., 1998) occur in two different field relationships which show also distinct chemical trends (Fig. 3a-d). One set of ferrodiorite typically lacking fayalite occurs up to 400m wide sheets continuous over several kilometres at the granitoid-anorthosite interface (Fig. 1c). These foliated ferrodiorites share gradational margins with the BZGs. In addition, N-striking ferrodiorites with intermediate Zr contents (Fig. 3a-d) form steeply-dipping tens-of-cm wide dykes that crosscut the margin-parallel foliation in anorthosites in the southern part of the massif margin (Fig. 2b; Bhattacharya et al., 1998; Nasipuri et al., 2011). These ferrodiorite dykes exhibit sharp contacts with anorthosite and are invariably highly sheared. Both occurrences of ferrodiorite taken together are inferred to be residual melts of polybaric anorthosite crystallisation (98% fractional crystallization; Nasipuri et al., 2011) from high-Al gabbroic parent melts that were contaminated by crustally-derived BZGs (Bhattacharya et al., 1998; Nasipuri et al., 2011). Due to melt-induced strain localisation, some of the ferrodiorites (residual melts) occurring as discontinuous films/pods within plagioclase aggregates (cumulates) were segregated into shear zone hosted ferrodiorite dykes (Fig. 2b) in response to far field stresses (Nasipuri et al., 2011). Based on mineralogy and whole rock geochemistry, the ferrodiorites can be classified as (i) fayalite-bearing ferrodiorite, (ii) ferrodiorite with anorthosite plagioclase xenocrysts, (iii) high-Ti ferrodiorite (TiO_2 6.75 wt%), (iv) fayalite-absent ferrodiorite, and (v) ferromonzodiorite.

Trace element abundances of the BZG's, anorthosite and ferrodiorites are starkly contrasting (Fig. 3c-d; Bhattacharya et al., 1998). In the BZGs, the Y, Th and Zr whole-rock

abundances are 30–160 ppm, 10–53 ppm, and 332–807 ppm respectively. In the fayalite-absent ferrodiorites, the corresponding values are 74–237 ppm, 64–189 ppm, and 4500–5220 ppm, respectively. The fayalite bearing ferrodiorite samples have highest concentrations, e.g., Y: 131–237 ppm, Th: 64–189 ppm and Zr: 4203–5512 ppm while the anorthosite, plagioclase xenocryst bearing and high-Ti ferrodiorites have the lowest concentrations, e.g., Y: 100–132 ppm, Th: 0–11 ppm, and Zr: 185–4582 ppm. By contrast, the Y, Th and Zr whole-rock abundances in anorthosite are 0–6 ppm, 0–5 ppm and 8–37 ppm, respectively.

Dobmeier (2006) suggests the N-striking shear zones developed in the ferrodiorite dykes and associated folds on the margin-parallel foliation are contemporaneous with the Pan African *sensu lato* NNW-SSE shortening that affected the crustal domain hosting the Balangir intrusive complex. By contrast, the BZGs are formed by incongruent melting of the basement gneisses (of unknown origin) that host the anorthosite complex, e.g., anatectic gneiss → Grt ± Opx ± Cpx + melt (BZG) (Nasipuri et al., 2011).

Garnets in these ferrodiorites are of two types, e.g., coronal (Fig. 2c; Bhattacharya et al., 2021) and non-coronal varieties (cf. Nasipuri et al., 2011). In the less intensely deformed ferrodiorites, the plagioclases are dotted by beads or aggregates or beads of post-tectonic coronal garnets (Fig. 2c; Bhattacharya et al., 2021). Thermo-barometry (700–920 °C) in the assemblage orthopyroxene/clinopyroxene – plagioclase ± quartz and garnet (both coronal and non-coronal varieties) yield peak P-T conditions of 850–920 ^{o}C and 6–8 kbar (Mukherjee et al., 1986; Mukherjee, 1989; Prasad et al., 2005; Nasipuri et al, 2011; Bhattacharya et al., 2021) in the intrusives neighboring the anorthosite-granitoid interface.

From two ferrodiorite samples Krause et al. (2001) reported discordant dates derived from zircon grains described as “long-prismatic and show the faint fine-scale oscillatory zoning typical for magmatic crystallisation, with some poorly luminescent thin overgrowths of metamorphic origin”. The upper intercept age (933 ± 32 Ma) is inferred to be the age of emplacement of the ferrodiorites; the lower intercept age at 515 ± 20 Ma overlaps with the concordant U–Pb titanite date of 516 ± 1 Ma obtained by Mezger and Cosca (1999) in calc-silicate gneisses bordering the massif (Krause et al., 2001). Vadlamani (2019) determined a Sm-Nd isochron age (495 ± 5 Ma) of combined anorthosite-garnet in two samples (PN 581e, PN 604), with Nd_i of 0.51150±0.00003 and MSWD of 2.9 (n = 4). Vadlamani (2019) also obtained an isochron age (481±12 Ma, with Nd_i of 0:511555± 0.00005 and MSWD of 0.02, with n = 3) from the ferrodiorites (PN 581e and PN 589), garnet fraction and its leachate. It is however unclear from the descriptions provided by Vadlamani (Fig. 4, 2019), if the garnets in

the anorthosite (PN 604) and the ferrodiorite (PN 589) are texturally older non-coronal garnets or texturally younger coronal garnets.

2. ZIRCON MORPHOLOGY, INTERNAL STRUCTURE AND CHEMISTRY

2.1 Sample description

Three representative BZGs (BG-4, 5 and 7) and one ferrodiorite dyke (BG-1B) lacking fayalite, were examined in detail.

The BZGs are structurally (Fig. 2a) and mineralogically similar (Fig. 4a, c). The rocks exhibit a single tectonic fabric (margin-parallel foliation) defined by quartz lentils, and drawn-out grains of recrystallized orthopyroxene >> clinopyroxene at the margins of the lentils in a dynamically recrystallized matrix of plagioclase and K-feldspar (Fig. 4c). Ilmenite, apatite, biotite and zircon are accessory minerals. The margin-parallel foliation wraps around xenoblastic garnet porphyroblasts with strongly embayed margins; the margins of the garnets are mantled by double-layered corona, with plagioclase and orthopyroxene forming the inner and the outer collar, respectively (Fig. 4c). The textures are discussed in detail by Prasad et al. (2005). The fabric-defining linear aggregates of pyroxenes can be traced to the outer collar of the double-layered corona around the pre-tectonic garnet porphyroblasts (Fig. 4c). This implies that garnet decomposition to orthopyroxene-plagioclase was broadly pre- to syn-tectonic with respect to the margin-parallel foliation.

The N-striking sheared ferrodiorite dyke BG-1B (Fig. 2b; 4b, d) truncates the margin-parallel foliation in anorthosite. The rock is substantially finer-grained than the BZGs and comprises a dynamically recrystallized matrix of orthopyroxene, clinopyroxene and plagioclase as the dominant minerals; quartz, ilmenite, pyrrhotite; apatite and zircon are accessory phases. Some of the orthopyroxene grains are prismatic in shape and define the shear zone fabric in the ferrodiorite (Fig. 4d). Circular to elliptical shaped garnets occur within the ferrodiorite (Fig. 4d); these garnets are not decomposed to pyroxene-plagioclase aggregates (Fig. 4d) as in the BZGs (Fig. 4a). Another textural type of garnets, broadly idioblastic to sub-idioblastic in shape, occurs as continuous films along the anorthosite-ferrodiorite interfaces (Fig. 4b). These garnets, discussed in detail by Nasipuri et al. (2011) and Bhattacharya et al. (2021), are post-tectonic with respect to the shear zone fabric as well as the margin-parallel foliation in anorthosite (Fig. 2b, 4b).

2.2 **Internal features in zircons**

The morphologies and internal structures of zircons in the BZGs and the ferrodiorite were examined using backscatter electron (BSE) imaging and cathodoluminescence (CL) imaging (Fig. 5, 6) performed at 40 nA current, 15 kV extraction voltage. In the garnet-bearing BZGs, zircon grains are lodged in garnet-pyroxene aggregates, and not in the quartzofeldspathic matrix (Fig. 4a). The zircon grains are abundant and large (50–300 μm long), and euhedral in shape with well-faceted margins; subhedral grains are rare (Fig. 5a-c). The zircon grains have two parts, e.g., an oscillatory zoned core that is delimited by un-zoned to thinly-zoned mantles having low CL response (Fig. 5a-c). In BSE and CL images, zircons exhibit complementary shades (e.g., Hanchar and Miller, 1993). The relative sizes of the oscillatory zoned core and the chemically-homogenous mantle vary considerably among grains in a sample, and between different samples (Fig. 5a-c). The mantles exhibit radial fractures (visible on BSE images) that barely extend into the cores (e.g., Fig. 5b, Zrn 6c.2, 6c.5, 6c.9 and 6c.24). Both the oscillatory-zoned cores and the chemically-homogenous mantles contain micro-pores in varying proportions (Fig. 5a-c).

The cores are invariably embayed, and the oscillatory zones in the embayed cores terminate against the mantles that exhibit well-faceted boundaries (e.g., Fig. 5a, Zrn 5a.5, 5b.13). In CL images, the core-mantle interfaces are sharp (shown by white arrows in Fig. 5a-c). In the zircons, veins and apophyses continuous with the mantles protrude into the cores, and are discordant to the oscillatory zoned cores (shown with black arrows in Fig. 5b, c; Zrn 7a.15, 7b.18, 6c.24, 6c.9).

In the BZGs, zircon hosted within the garnet porphyroblasts, pre-tectonic with respect to the margin-parallel high-T foliation, is rare. In the border zone granitoid BG-7 (Fig. 6), garnet-hosted zircons have similar CL features as the ones in the dynamically recrystallized matrix (Fig. 5c) in the BZGs, except that the mantles are thinner relative to the oscillatory-zoned cores (Fig. 6c, Zrn 7b.20).

In the ferrodiorite dyke BG-1B, zircons are abundant (Fig. 5d), but rarely with the above-mentioned features (Fig. 5d, Zrn 1Ba.5). The morphologically different types of zircons occur within the dynamically recrystallized plagioclase-pyroxene matrix, but are not hosted in the garnets. The dominant proportion of zircons are anhedral and large (100–600μm diameter), and resemble the “cauliflower”-shaped zircon grains (cf. 25–27 in Fig. 2 of Corfu et al., 2003; Peucat et al., 1990) (Fig. 5d, Zrn. 1Ba.1, 1Bb.3, 1Bb.4). The shapes of the cauliflower-shaped zircon grains are best described as angular with sub-rounded margins. These zircon grains contain profuse micropores, and irregular patchy CL responses separated by clear lines in different CL images (Fig. 5d, Zrn 1Ba.1, 1Bb.3, 1Bb.4 and 1Bc.4). The

internal structures of these zircon grains are similar to those described by Peucat et al (1990; Plate 1, no. 13) in basic granulite from the Sobradu Unit in the Cabo Ortegal high-pressure nappe, north-western Spain, in eclogite facies garnet bearing quartz-mica schists of Sikinos and Ios Island, Greece (Poulaki et al., 2021), and some zircons of the granulite facies meta-mafic/ultramafic rocks of the Ivrea Verbano Shear Zone, Southern Alps, Italy (Langone et al., 2018). Other studies that have notably reported cauliflower zircons from high grade terranes include Bernard-Griffiths et al. (1991), Fu et al. (2012) and Pystina and Pystin (2019). By contrast, there is a second zircon population which is smaller sized (Fig. 5d, Zrn 1Ba.5), sub-idioblastic, and characterised by oscillatory zones. The margins of the oscillatory zoned cores in these zircons are bordered by thin (<5 μm) mantles having low, near homogeneous CL intensities (Fig. 5d, Zrn 1Ba.5). By contrast to the zircons in the granitoids, the intensities of BSE and CL images are not complementary.

2.3 **Element zoning in zircon using EPMA and LA-ICP-MS**

X-ray element maps for Hf, U, and Y in representative zircon crystals in the rocks (Fig. 7) were determined using a Cameca SX-Five Electron Probe Microanalyzer (EPMA) at the Department of Earth Sciences, IIT Bombay. The X-ray elemental maps were obtained with 200 nA current, 15 kV acceleration voltage and 100 ms dwell time; grains Zrn 5c.6, 5c.9 in BG-5 and Zrn 1Bc.4 in BG-1B (Fig. 7) were mapped using 150 nA current. The elemental maps for Y, Hf, and U were determined for zircon grains in two BZGs (BG-5, 6) and the ferrodiorite BG-1B (Fig. 7). For the analytical conditions, Nb and Ca contents for the zircon grains in the samples were below detection limit; hence X-ray maps for these elements could not be obtained. The Th, U and Pb contents in the zircons were semi-quantitatively measured during LA-ICP-MS U-Pb dating (Supplementary Material[1]) of the zircon grains in three BZGs (BG-4, 5 and 7) and the ferrodiorite BG-1B. All analytical conditions are listed in the Supplementary Material[1]. It should be noted that Y, Hf and U maps are shown to access the relative changes in composition within individual grains, rather than for quantitative analyses. In particular, the lower sensitivity of U on the X-ray elemental maps should be noted.

In the BZGs, the oscillatory zoned zircons exhibit variable abundances of Y, Hf, and U (upper and middle panels in Fig. 7). Zoning patterns of zircons in CL and BSE images are most reliably matched by Yttrium abundances (Fig. 7), and to a lesser extent by Hf. Higher abundances of Hf and Y match the CL dark zones and BSE bright zones in the zircon grains. Fine-scale oscillations in CL images do not show up on the X-ray elemental maps (Fig. 7), possibly because the step sizes chosen were larger than the width of the oscillatory zones.

The margins in the BZG zircons are chemically homogeneous, but chemically distinct from the oscillatory zoned cores (Fig. 7; grains 5b.8, 13, 20, 6c.6, 9). The most notable difference is in Y abundances, i.e., the mantles have lower Y contents relative to the oscillatory-zoned core in BG-5 and 6 (Fig. 7). Though not pronounced, Hf abundances in the mantle are marginally higher relative to the cores (Fig. 7, grains 5b.8, 20).

The modally subordinate, finer-sized, oscillatory-zoned zircon grains in the ferrodiorite dyke sample BG-1B (lower panel; Fig. 7) exhibit Y zonation that mimics the BSE bright and CL dark zones (Fig. 7; lower panel, grains Zrn1Bc.3, Zrn1Bc.4); this further substantiates that Y content influences BSE and CL intensities. However, the euhedral zircon in the ferrodiorite show uniform abundances of Hf and U, unlike in the BZGs, and the fine-scale oscillatory zones within these grains are not evident on the X-ray elemental maps. The population of "cauliflower" zircon in the ferrodiorite BG-1B (Fig. 7, lower panel) appear homogenous in the X-ray elemental maps for U and Hf, but Y contents vary within the grain, and coincide with darker CL response domains.

4.3. Quantitative orientation analysis of internal zircon structures

Electron backscatter diffraction (*EBSD*) analysis was conducted on selected zircon grains to explore to what extent radiation damage, crystal plastic deformation, fracturing and/or replacement reaction may have influenced the chemical and geochronological data. EBSD allows full (all crystallographic axes) quantitative crystallographic characterisation of a mineral with information on spatial variations. For EBSD analyses, already polished thin sections were additionally mechano-chemically polished with colloidal silica and carbon coated with a thin carbon coat (3-5 nm). Data was acquired at the LEMAS centre (University of Leeds) using the Oxford Instruments Symmetry EBSD Detector on a field emission gun FEI Quanta 650. Data were acquired in regular grids with a step size of 0.5 μm at 30 keV. Data were processed using AztecCrystal (Oxford Instruments). The degree of potential radiation damage is readily assessed using EBSD: if radiation damage is severe, the crystal lattice does not exist anymore and no diffraction data can be collected. The degree of lattice distortion is assessed using profiles of orientation changes and with Grain Reference Orientation Deviation (GROD) angle maps (Figs. 8, 9) which takes the average orientation of each grain and shows the colour coded relative misorientation for each pixel, with misorientation being defined as the smallest possible misorientation. Abrupt changes signify sudden lattice changes either originating from crystal plastic deformation, growth or fracture related zircon block rotations and healing (e.g. Rimša et al., 2007; Tretiakova et al., 2017).

Crystal plastic deformation results in a systematic change in orientation according to the slip system activated (e.g., Reddy et al., 2007; Piazolo et al., 2012). Lower hemisphere pole figures are used to highlight the extent and nature of lattice dispersions of individual grains. Inverse pole figures are used to assess the nature of low angle rotation axes associated with lattice distortions.

We present data from representative zircons occurring in the BZGs and the ferrodiorite dyke. All zircons investigated do not show any signature of significant radiation damage; they are all crystalline throughout (e.g., Fig. 8, 9). Zircons from the BZG exhibit little orientation changes within individual grains (Fig. 8) although subtle systematic orientation changes occur where oscillatory zoning is present (Fig. 8ai, bi). The mantles are either homogeneous in orientation, similar to the CL signatures, or can exhibit slight systematic variations parallel to facets. However, some orientation change is still noticeable reaching up to 2° relative to the mean orientation. Profiles show little systematic changes (Fig. 8aiv, 8biv), although low angle misorientation axes are systematic in the core. Low angle misorientation axes in the mantle are either similar to the core but less well aligned (Fig. 8aii), or distinctly different while still less well aligned (Fig. 8bii). The large zircon grains within the ferrodiorite dyke are distinctly different in their quantitative crystallographic orientation relationships. These grains show distinct, local, and systematic sudden changes in orientation. This is seen as change in colour in GROD maps and subgrain boundaries, i.e., orientation changes of up to 2° over 0.5 μm as well as smooth continuous change in orientation (Fig. 9aii, bii; aiv, biv). Large grains show an orientation dispersion of up to 8° relative to the mean orientation (Fig. 9aii, bii). If the grain is irregular in shape, protrusions show the most significant change in orientation and distinct lines of sudden orientation change (Fig. 9a, b). The pole figures of the respective whole grains show well defined small circle dispersions (Fig. 9 biii) typical for crystal plastic deformation. There is a clear spatial correlation between areas and lines (i.e., subgrain boundaries) of high lattice distortion and with distinct CL signatures (Fig. 9a, b). The thin, light CL mantles are asymmetric (Fig. 9ai, bi) and in case of zircon grain Zrn 1Bb.4, subgrain boundaries are mainly perpendicular to the grain-surrounding interface (cf. red arrows). Low angle misorientation axes and subgrain boundaries are well defined in the centre but more dispersed in the mantle area (Fig. 9). An example of a smaller grain shows only a rare subgrain boundary (Fig. 9c), while the rest of the grain shows little orientation change except for one

edge (Fig. 9c). Overall orientations vary much less than for the large grains (e.g., maximum orientation of 2°).

3. TI-IN-ZIRCON THERMOMETRY

Ti-in-zircon thermometry was applied to estimate temperatures (Fig. 10a) in the oscillatory zoned cores and chemically distinct mantles in multiple zircon grains in two BZGs (BG-5, BG-7) and in the cauliflower-shaped zircons in the ferrodiorite dyke (BG-1B). The Ti contents in zircon were determined simultaneously with U-Pb isotope spot analyses using a 25μm beam diameter in LA-ICPMS (see below). Elemental data were normalised using NIST612 as external standard and ^{29}Si as internal standard.

Ti-in-zircon temperatures were obtained using the thermometric formulations of Watson et al. (2006) and Ferry and Watson (2007). Since rutile is absent in the rocks, i.e., $a(TiO_2) < 1$, and ilmenite is the stable TiO_2-bearing phase, temperatures were computed using $a(TiO_2)$ values of 0.7 and 0.9 suggested by Menegon et al. (2011) and Peterman and Grove (2010). In each of the BZGs, the T values estimated from the core and the mantle considerably overlap (700–950 °C; Fig. 10a). The Ti-in-zircon temperatures compare favourably with the zircon saturation temperatures (850–950 °C; Fig. 3b) for BZGs computed using the whole rock chemical data in Bhattacharya et al. (1988). The ferrodiorite dyke zircons could not be compared because the M values exceed the limits of the diagram proposed by Harrison and Watson (1983) (shown as gray shaded box in Fig. 3b). In the BZGs, the mantles, at least for BG-7, yield temperature (700–750 °C) comparable to the lowermost range of T values obtained from the cores. In the ferrodiorite dyke BG-1B, the Ti-in-zircon temperatures are clustered between 700 and 750 °C, and are comparable with the T values retrieved from BG-7 mantles. The ranges of Ti-in-zircon T values in the three samples taken together are comparable (Fig. 10b) with the range of metamorphic T values (700–950 °C) obtained from the different formulations of Mg-Fe exchange thermometers, e.g., orthopyroxene-garnet, clinopyroxene garnet and two-pyroxene pairs, by several authors (Mukherjee et al, 1986; Nasipuri et al., 2011; Bhattacharya et al., 2021).

4. LA-ICP-MS U-Pb ZIRCON GEOCHRONOLOGY

The four samples (BG-1B, 4, 5 and 7) were dated at the the Plateforme GeOHeLiS, Géosciences Rennes, University of Rennes using an Agilent 7700x, Q-ICP-MS combined with an ESI NWR193UC, Excimer laser. The isotope analyses of the zircons were conducted in >1mm thick glass-mounted rock slices, using a 25 mm round spot with a repetition rate of

4Hz and a fluence of 6 J/cm^2. The details of the analytical conditions, instrument operation parameters and data reduction procedure are provided in Banerjee et al. (2022a, b; summarised in Supplementary Material[1]). The analytical data and the dates are presented in the Supplementary Material[1]. The concordia diagrams obtained with IsoplotR (Vermeesch, 2018) are shown in Fig. 11. Throughout the text, figures and tables, dates are reported with their 2σ uncertainty without and with systematic uncertainties propagated (Horstwood et al., 2016).

Ellipses of zircons sequestered within pre-tectonic garnets with respect to the margin-parallel foliation are shown on Fig. 12 together with the discordia lines for the 4 samples. Raw signal is reduced using Iolite v4.7 (Paton et al., 2011). Given most zircons have complicated CL zonations, it is important to avoid data-mixing from different domains. Therefore, the isotopic ratio signal was monitored carefully against time for each analysis. If an abrupt change occurred only the first part of the signal was kept to ensure a match between results and CL image.

Concordance is defined as (^{206}Pb/^{238}U Age/ ^{207}Pb/^{235}U Age) * 100, and for a large part of the spots analyzed, dates could be looked as concordant, 61 spots out of 138 have concordance > 98%. However, we do not think that these dates could be used as concordant dates. Instead, we argue that for the 4 samples, ellipses are mostly discordant and aligned on a discordia line with upper and lower intercept of ca. 980 Ma and 495 Ma respectively (Fig. 12a).

In the granitoid BG-4, twenty spots were analyzed in ten grains which define a discordia line with upper intercept at 977 ± 20/21 Ma and lower intercept at 485 ± 57/57 Ma. The spot analyses in the embayed cores with oscillatory zones yield older dates as compared to the homogenous mantles.

Forty-three spots analyzed in seventeen grains from granitoid sample BG-5 yielded a discordia line with upper intercept at 968 ± 26/27 Ma and lower intercept at 497 ± 16/17 Ma. Zircon cores with oscillatory zones yield older dates as compared to the mantles truncating them; however, in a few grains (Fig. 11; BG 5 Zrn 5a.1 and 5a.6) with cores with CL dark response, younger dates are obtained from the cores as compared to the surrounding mantle.

A discordia line with upper intercept at 1001 ± 38/39 Ma and lower intercept at 498 ± 27/28Ma is defined by thirty-seven out of thirty-nine spots analyzed in twenty-one zircon grains from granitoid sample BG-7. Zircons also have oscillatory zoned cores with wide homogenous mantles truncating them, these cores yield older dates compared to the surrounding mantles (Fig. 11). However, in some zircon grains, the cores furnish younger

dates as compared to the mantle (Fig. 11; BG 7, Zrn 7a.1, 7a.2, 7a.5, 7a.6, 7a.13, 7a.15, and 7a.19). Also, in some of the grains, the younging of dates obtained from a grain (e.g. Zr 7b.3x, Zr 7b.20) is independent of the distance of the analyzed spot from the grain edge.

In the ferrodiorite dyke BG-1B, thirty-five spots were analyzed in five grains. Thirty-four of the spots define a discordia with upper intercept at 980 ± 82/82 Ma and lower intercept at 488 ± 25/26 Ma. The CL bright domains generally yield older dates than the CL dark zones; in the euhedral oscillatory zoned zircon grain (Fig. 11; BG 1B, Zrn 1Ba.5) dates though variable, do not follow a core-mantle trend.

In granitoid BG-7, three zircon grains hosted within garnet porphyroblasts pre-tectonic with respect to the margin-parallel foliation were analysed (Fig. 6, Fig. 12). Ellipses plot along the array of the four discordia lines retrieved from the four other samples independently (Fig. 12). We therefore assume that the processes that caused the discordance were common to zircon grains both in the recrystallized matrix as well as in the garnet porphyroblasts that pre-date the margin-parallel fabric in the intrusives bordering the anorthosite pluton.

The concentrations of the parent elements Th and U within these zircon grains were calculated; barring one spot (in BG-4), the Th/U ratios are typically >0.1, and up to 4.45 in BG-5. The overwhelming number of spots yields values in the range 0.15–2.25 (Supplementary File[1]), indicating a plausible magmatic origin for these zircons.

5. DISCUSSION

In the following section, we discuss the different textures seen in the zircons and their link to the tectonometamorphic evolution of the area studied. Figure. 13 (a-d) provides schematically the interpreted anorthosite-ferrodiorite evolution at ~495 Ma in the Balangir pluton and the link to the observed textures in the zircon.

5.1 The origin of oscillatory-zoned cores in zircon in the BZGs

Four distinct features in zircon grains in BZGs can be distinguished, (1) cores with sharply-defined oscillatory zones of varying Y, Hf and U abundances; these cores also have embayed margins, (2) the oscillatory zones in the cores are abruptly truncated by irregularly shaped, chemically homogenous mantles, (3) the mantles with well-faceted margins preserve coherent crystallographic orientations with the oscillatory-zoned cores (e.g., Zrn 7b.3x, Zrn 5b.20, Zrn 5a.5; Fig. 5 and 6), and (4) “veins” with low-CL intensities are physically

continuous with the mantles partially transect within the oscillatory zones in the embayed cores.

Diffusivity experiments in zircon at high temperatures (T > 1100 °C) are consistent with the following inferences: (a) HREEs diffuse faster than the larger LREEs that are incompatible with the tight zircon structure (Cherniak and Watson, 2003, 1997a); (b) the REEs diffuse 3–5 orders of magnitude faster than tetravalent cations (Cherniak and Watson, 2000, 2003; Cherniak et al., 1997b); (c) Hf diffuses more rapidly than U or Th, but slower than the REEs (Cherniak and Watson, 2003); (d) the closure temperature for Pb in zircon computed using the experimentally determined diffusion parameters is 900 °C (Cherniak and Watson, 2001); (e) Bloch et al. (2022) determined Ti diffusion parallel to c-axis in zircon to be 4–5 orders of magnitude more than diffusion perpendicular to c-axis at the experimental T values (1100–1540 °C), but increases to 7.5–11 orders at lower temperature crustal conditions (cf. Cherniak and Watson, 2007). However, extrapolations of these inferences based on the results of high-T experiments to lower-T crustal conditions are somewhat approximate (Cherniak and Watson, 2001, 2007; Cherniak et al., 1997)

In summary, the HREEs are among the fastest diffusing elements in zircon. The ionic radius of Y^{3+} is comparable with Tb^{3+} among the HREEs (Van Gossen et al., 2017). The preservation of the sharply-defined Y zoning profiles in the oscillatory zoned zircon in BZGs and the ferrodiorite BG-1B (Fig. 7) suggests that the pristine element variations acquired during crystallization of the cores were either largely unaffected or were partly modified by lattice diffusion. Lattice diffusion did not erase the Y variations across tens-of-microns wide oscillatory zones and across the >50 μm and up to 150 μm diameter embayed cores at the metamorphic temperatures 700–930 °C obtained from mineral thermo-barometry and Ti-in-zircon thermometry (Fig. 10a, b). The length scale of lattice diffusion of the slower-moving tetravalent elements such as U and Hf (Fig. 7), and by extension Th and Pb, are likely to be shorter relative to Y. The uppermost range of the metamorphic temperatures is barely comparable to the blocking temperature of Pb diffusion, 900 °C. Based on the preservation of element zonation, especially sharply-defined Y zonation, the length scale of diffusive migration of the elements was short (in tens-of-micron scale) presumably because the high T conditions prevailed for short time scale (Cherniak et al., 1997a; Williams et al., 1995; Flowers et al., 2006), and was inadequate for the chemical homogenisation of the trace elements across the oscillatory zones. For the lower temperature end (700–750 °C; Fig. 10a), the length scale of intra-crystalline diffusivity is likely to be shorter (couple-of-microns at best; undetected in this study) and is unlikely to erase the inherited zoning profiles, even if

diffusion persisted over longer time scales. We infer therefore that the oscillatory zoned cores of zircon in the BZG matrix (BG-4, 5 and 7) as well as in the garnet porphyroblasts (in BG-7) and in the ferrodiorite dyke BG-1B are originally magmatic (Fig. 13a, stage 1). However, the range of U-Pb dates and the degree of discordance (Fig. 11, 12) implies that the pristine isotopic ratios (Figs. 5–7) were variably modified by subsequent processes, independent of the Th/U ratios of the parent element, U and Th.

5.2 **The origin of mantles around oscillatory-zoned cores in zircon in BZGs**

In the granitoids (Fig. 13a), the chemically-homogenous mantles are commonly asymmetric (i.e., different thickness at different edges) and their interface to the core is irregular (Fig. 5a-c). The mantles are distinct in their CL and BSE signature from the core. Importantly they are relatively homogeneous as shown in their CL signature, BSE signature (Figs. 5, 6) as well as trace element content (Fig. 7). Despite this difference, both the cores and the mantles share coherent crystallographic orientation (Fig. 8). The asymmetric nature of the mantles, their paucity of chemical zonation, the presence of micropores, the sharp irregular interface to the core which truncates older oscillatory zones in the cores in zircon crystals suggest that fluid/melt-driven processes led to the formation of these mantles. We interpret that these mantles formed by advection-accommodated interface-coupled dissolution-precipitation process (Vonlanthen et al., 2012; Kelly et al., 2017; Poulaki et al., 2021). The process involved fluid/melt-driven dissolution of the core that caused embayment in the oscillatory-zoned cores, followed by the precipitation of the epitaxial mantles that grew by preserving the crystallographic orientation of the zircon cores by the process of interface-coupled precipitation (Fig. 13b (this study); Vonlanthen et al., 2012). In the metamorphic community this process is often referred to as fluid/melt mediated interface coupled replacement reactions (Putnis, 2009; Spruzeniece et al., 2017). Our interpretation is supported by EBSD data, in particular the mantles show less defined misorientation axes and less defined patterns of orientation changes (Fig. 8). Spruzeniece et al. (2017) showed that this is an expected feature of fluid-mediated interface coupled replacement reactions.

5.3 The origin and co-existence of large cauliflower-shaped and small sub-idioblastic zircon in the ferrodiorite dyke

Within the sheared ferrodiorite dyke BG-1B the abundant zircon grains occur as two populations; namely (a) large (>200µm diameter) cauliflower-shaped zircons with profuse micropores, distinct subgrains (Fig. 5d, Fig. 9) – features lacking in zircons in BZGs – and

(b) a subsidiary population of smaller zircon crystals with embayed oscillatory-zoned cores. Both populations exhibit asymmetric thin (<5μm wide), chemically-homogeneous and CL signature distinct rims, a feature similar to zircons in BZGs. At the same time, the ferrodiorite sample has high whole-rock Zr values (1500–5000 ppm; Fig. 3c-d; Bhattacharya et al., 1998).

Theoretical calculations by Nasipuri et al. (2011) indicate that the measured Zr abundances in the ferrodiorites cannot be explained by closed system high-degree (>98%) of fractionation of anorthosite from high-Al gabbro parent magma. To attain the measured Zr abundances in the ferrodiorites, the anorthosite residual melts need to be contaminated by Zr-richer felsic magma (BZGs) during crystal fractionation (Bhattacharya et al., 1998; Nasipuri et al., 2011). Alternatively, the high Zr abundances may be explained by the selective entrainment of zircon xenocrysts from the protoliths of the intruded ferrodiorites or BZGs, or by assimilation of zircon-bearing felsic rocks that host the ferrodiorites. But anorthosite-leuconorite in the Balangir pluton does not contain zircon, and enclaves of felsic rocks (BZGs and/or basement gneisses) are lacking in the anorthosite-hosted ferrodiorite dykes.

Based on high Zr abundance and given the similarity of internal structures of the small, oscillatory zoned zircons in ferrodiorites and BZGs, we propose the entrainment of zircon in ferrodiorites was possible via mixing with BZG melts, and these entrained zircon xenocrysts are unlikely to have dissolved in the ferrodiorite residual melts (Fig. 13c, stage 2). Given the low Zr solubility in the ferrodiorite melts, complete zircon dissolution is unlikely, allowing entrained zircon to survive.

In contrast to these small xenocrysts, the origin of the large cauliflower-shaped zircons which do not exhibit any of the typical oscillatory zoning is on a different footing. These largely chemically homogenous zircons with profuse micropores and subgrain boundaries may have formed by any of the three processes: (a) Lattice diffusion and Pb loss that completely obliterated the pristine character of the zircon xenocrysts; (b) direct crystallization of zircon from the ferrodiorite melt or (c) melt-mediated dissolution of older xenocrysts and precipitation of zircon lattice with different isotopic signature. Lattice diffusion (process a) is unlikely because this process should have affected the small xenocrystic population as well, which is not the case. Direct crystallization from the melt is a possibility but would be expected to yield homogeneous ages of the age of emplacement and crystallization as well as oscillatory zonation. Our data show that ages are highly variable, even within a single CL domain (Fig. 11d). We suggest instead pre-existing, inherited grains have been completely replaced and grown upon following a melt mediated replacement reaction (Fig. 13d, stage 2). This would necessitate the pre-existing zircons to be in chemical

disequilibrium with the host melt i.e., the mafic/ultramafic ferrodiorite melt, and, to result in extra growth, this melt was Zr enriched.

Progressive fractionation of anorthosite-leuconorite from parental melts contaminated by BZGs (Bhattacharya et al., 1998; Nasipuri et al., 2011) would cause (i) the volume fraction of the residual ferrodiorite melt to decrease due to polybaric fractionation of the plagioclase crystal mush (cf. Fram and Longhi, 1992), and (ii) the enrichment of plagioclase incompatible elements such as REEs, Zr, U and Th in the decreasing volume of ferrodiorite residual melts (Bhattacharya et al., 1998; Nasipuri et al., 2011). Once the Zr abundance in the melt exceeds the solubility threshold, excess amounts of Zr would be available for zircon growth (Fig. 13d, stage 2). This melt would be in chemical disequilibrium with the entrained zircons; hence replacement reactions would take place. Due to high Zr abundance, and ease of nucleation at the surfaces of pre-existing zircon (entrained from country rocks) further growth would be on the replaced pre-existing zircon crystals resulting in large sizes. Replacement reactions commonly results in highly porous material. These features are well documented in the cauliflower zircons (Fig. 5d). In rare cases, a remnant of a xenocryst is still clearly visible (Fig. 9c). As these ferrodiorite melt hosted dykes are being sheared and are cooling and crystallizing at the same time, the resultant zircon grain shape is highly heterogeneous and mainly anhedral. The grain grows within an increasingly crystalline and continuously changing solid grain microstructure. Once the solid crystal fraction is high and melt is heterogeneously distributed, continued shearing results in local grain impingement and stress transfer which results in the observed substructures with characteristics of dislocation creep (Fig.9, 13d).

Both populations of zircons were subject to a late-stage replacement reaction forming the observed thin, but distinct asymmetric mantles (e.g., Fig. 9 b, c). The asymmetry points to the fact that melt availability was limited and heterogeneously distributed, i.e., only along some of the grain boundaries. EBSD data supports such a replacement process as subgrain boundaries in the mantles are developed dominantly at right angles to reaction interface (Fig. 9; red arrows).

5.4 Evidence for melt versus fluids

Several lines of evidence suggest that the interpreted interface coupled replacement reactions did not involve CO_2-H_2O fluids. First, both the BZGs and the ferrodiorites, in general, and the N-striking BG-1B ferrodiorite dyke, in particular, comprise anhydrous minerals, barring accessory amount of biotite hosted within the garnet porphyroblasts and in the matrix.

Second, the ferrodiorite dykes occurs within the anorthosite pluton and does not extend into the basement gneisses into which the Balangir anorthosite complex intruded. And finally, experimental determinations indicate the Zr has very low solubility in aqueous fluids (Chen et al., 2023). Based on mesoscale structures, Dobmeier (2006) suggests the deformation of the anorthosite pluton/BZGs and the N-striking ferrodiorite were contemporaneous with NNW-SSE crustal shortening. Nasipuri et al. (2011) contend the N-striking shear zones are exclusively associated with the ferrodiorite dykes due to the localisation of deformation strain by small amounts of ferrodiorite residual melt pods within a deforming plagioclase crystal mush (Fig. 13a, c).

Based on analyses of deformation microstructures, Nasipuri and Bhattacharya (2007) suggest that interstitial melts were present in the initial stages of deformation of the plagioclase crystal mush, although deformation outlasted crystallization of the pluton. Bhattacharya et al. (2021; Fig. 3b) demonstrate trains of end-to-end touching euhedral long-prismatic orthopyroxene crystal wrapping around deformed plagioclase phenocrysts in ferrodiorites, similar to magmatic flow textures. The evidence, taken together, suggest the margin-parallel foliation and the N-striking shear zones nucleated sequentially, but closely in time, and melts were present at least during the early stages of deformation of the intrusives (Fig. 13a, c). It stands to reason therefore that melts, rather than aqueous fluids, were involved during the dissolution of zircon cores and the precipitation of mantles (Fig. 13a-b, stage 1).

5.5 U-Pb systematics and the observed discordia

U-Pb dates in BZGs and the ferrodiorite, irrespective of the textural setting and the internal structure of zircons in the chemically diverse intrusives are smeared along a near-unique discordia line. Actually, plotted together the data (131 spots out of a total of 138) for all samples yielded intercepts of 493.8 ± 11.1/11.8 Ma and 978.8 ± 13.7/15.2 Ma with a MSWD of 0.95 indicating a statistically coherent population. In spite of considerable overlap of dates in the individual samples, the mantles around oscillatory zoned cores in zircons (in BZGs) tend to segregate towards the lower intercept (Fig. 11a-c). We suggest that the two intercept dates correspond to two stages of zircon growth, i.e., the upper intercept at ~980 Ma corresponds with the age of magmatic crystallization of the zircon vis-a-vis the intrusives, and the younger intercept age (~495 Ma) represents the age of fluid-induced high-T growth of epitaxial zircon mantles in BZGs and the cauliflower-shaped zircons in ferrodiorite (Fig. 13, stages 1 and 2). Krausse et al. (2001) obtained similar results (upper and lower intercepts

at 933±32 Ma and 515±20 Ma respectively) with ID-TIMS dissolution dating. Krausse et al. (2001) suggest Pb loss to account for the discordance in U-Pb dates, but the process responsible for the open system behaviour of Pb remained obscure.

In order to assess the causes for Pb loss several findings need to be addressed: (a) the large span of U-Pb dates and discordance degree (Supplementary File[1]), and (b) the Y, U, and Hf variations in the oscillatory-zoned cores (Fig. 7).

It may be argued that the near-unique discordia line for the samples is an artefact of mechanical mixing (carved out by depth-impingement due to Laser ablation) between the two end-member dates, ~980 Ma and ~495 Ma. Chew et al. (2021) suggested the discordant dates in zircon 823 (Chew et al., 2017) in the range 1.1 and 0.48 Ga (comparable to those in this study) were the result of mixing two age domains due to greater penetration (10-20µm) during laser ablation using LA-ICPMS, and Pb loss. In this study, the analyses were done *in situ* in grains with the short axes of the oscillatory zoned cores in BZGs varying between ~30µm (Fig. 5a; Zrn 5a.5; Fig. 5b, Zrn 6c.5) and at least up to 80µm (Fig. 5b, Zrn6c.6; Fig. 5c, Zrn 7a.15). An overwhelming number of grains have square to rectangular outlines, and exhibit weakly developed pyramidal faces (both the core and the mantle have near identical crystallographic orientations, Fig. 8). By implication, the ablated faces in most of the zircon grains are oriented at high angle to the c-axis rather than sub-parallel to c-axis as in mounted zircon grains that overwhelmingly lie on the prism faces terminated by pyramidal faces. If we consider that the zircon grains are hemispheres, the lengths of the short axes of the oscillatory zoned cores below the exposed surfaces vary between 15µm to at least 40 µm. In other words, for a majority of the larger zircon grains, the penetration depths of the laser beam within the *in situ* grains oriented oblique to the long axes were smaller than the depths for the oscillatory zoned cores. Thus, at least for the larger cores mixing of different age domains is unlikely. Further, examination of raw data did not show up evidence in favour of such a possibility, and therefore mechanical mixing of end-member dates as a means to explain the discordance appears to be untenable. But even if mechanical mixing was indeed a possible mechanism for age discordance, it still begs the question as to what is the significance of the two end-member dates.

For all zircons, results of EBSD (Figs. 8–9) confirm the high degree of crystallinity of all studied zircons. In zircons from the Jack Hills, Huijsmans et al. (2022) suggest that recrystallization is associated with bending and fading of oscillatory zones in Hf, U, Pb and Y, and the formation of recrystallization interfaces with < 2° misorientation. In the BZGs, the preservation of sharp zonations of the slowest moving Y (Fig. 7) and the lack of

misorientations (Fig. 8) seemingly rule out Pb loss induced by high-T recrystallization in oscillatory zoned cores in zircons if they were subject to metamictization (Cherniak and Watson, 2001; Marsellos and Garver, 2010) and therefore crystal lattice damage. Additionally, we also calculated the α-dosage for the analysed spots in the zircon grains from this study based on U and Th concentrations during 500 Ma which represent the alpha dose accumulated between 500 and 1000 Ma with U and Th content calculated at 500 Ma, and the other one is the alpha dose accumulated between 500Ma and present day with U and Th concentration at present day using the formulations of Murakami et al. (1991) (Supplementary File[2]). The α-dosage values for these zircons are well below the threshold of metamictization as given by Woodhead et al. (1991; 4.5.10^18 α event/gram) or beginning of defect connection at 3 10^18 α event/gram (Murakami et al., 1991). We therefore argue that the zircons in this study were non-metamict at 500 Ma and the present day.

For BZGs and the small sub-idioblastic zircons in the ferrodiorite dyke the absence of significant lattice bending and the lack of subgrains preclude Pb loss through pipe diffusion along subgrain boundaries and/or distorted crystal lattice (Reddy et al. 1997, Piazolo et al. 2012, 2016). For these zircons the paucity of concordant dates corresponding to the upper intercept – even from the centrally located, oscillatory zoned parts of the zircon grains in the BZGs and the ferrodiorite dyke (50–150 μm diameter) – suggest even in the apparently unmodified cores the pristine compositions of the zircons were subsequently modified. But the preservation of well-defined Y zonation (tens of micron wide at the most) in oscillatory-zoned zircon cores (Fig. 7), suggests it may be unrealistic to assume that lattice diffusion alone modified the pristine magmatic isotope ratios especially in the grain interiors. In addition, in a number of instances (Figs. 11, 12) U-Pb ages do not follow a decreasing age with proximity to the grain boundaries, which is inconsistent with a lattice diffusion related chemical modification. Clearly processes other than lattice diffusion led to modifications in the pristine isotope ratios of interiors of oscillatory zoned cores.

Varga et al. (2020) experimentally demonstrate that neo-crystallized monazites partly inherit the age of the precursor grains. Fougesouse et al. (2024) show that in situ melting resulted in significant modification of ages by an interface-coupled replacement process. During such replacement reactions (e.g., Putnis, 2009), a zircon in chemical disequilibrium with its surrounding will dissolve, and new zircon will be formed at the same interface from the chemically oversaturated fluid at the interface-fluid boundary. This fluid carries an isotopic chemical signature which is a mix between the original and the new fluid. The fluid reservoir for the zircon growth is likely to be limited and its exact chemistry i.e., the relative

ratio of the chemical signature of the original and new chemical composition is expected to be variable as this ratio depends on the local connectivity of the interface fluid to the matrix reservoir (see Fig. 13b). Since, different trace elements will diffuse in a fluid at different rates (e.g., Holycross and Watson, 2018; Zhang et al., 2010), the elements will be heterogeneously distributed in the fluid. The element/isotopic heterogeneity is likely to be more pronounced in silicate melts because of lower element diffusivity relative to aqueous fluids. Consequently, zonations may be preserved with the melt volume neighbouring the growing zircon grains. In addition, such replacement reactions result in crystals that exhibit pores and show non-systematic lattice distortions, distinct from lattice distortions induced by crystal plastic deformation (Spruzeniece et al., 2017).

We suggest that apparent, spatially heterogeneously distributed range of discordant analyses in the texturally diverse zircon grains, and the paucity of concordant dates in the younger zircon mantles are a direct result of a melt-mediated interface-coupled replacement reaction involving dissolution of original (oscillatory-zoned) zircon and reprecipitation of zircon mantles with a chemical signature originating from chemical mixture (Fig. 13b). In other words, the U-Pb isotope ratios of the younger mantles in zircon are aligned along a discordia limited by the isotope ratios of the 980 Ma zircon xenocrysts, albeit modified, and the isotope ratios of the melt-mediated replacement involving dissolution and epitaxially grown younger metamorphic mantles (~495 Ma) that partly inherited the isotope ratios of the, partially dissolved older cores. The proposed process explains the subtle lattice distortions observed in the areas of chemical modification e.g., mantles (Fig. 8), the high abundance of porosity and the intriguingly heterogeneous age distribution within the mantles themselves (Fig.11b, d). The heterogeneity of the chemical variations within the mantles provides a qualitative measure of the zircon to external-to-zircon melt connectivity within the rock. At high connectivity, one would expect very good chemical exchange at all stages of the dissolution-precipitation process allowing near homogeneous mixtures of ages. In contrast, low connectivity would result in high chemical heterogeneity due to very local chemically distinct “melt reservoirs”. Such low connectivity may be due to either very tight porosity pathways or an overall low zircon to melt ratio. Our data shows <5µm diameter sized pores (Fig. 5) suggesting good pore related connectivity; therefore, we suggest that the zircon-melt ratios were low.

A related question is: Why do the cores of the zircon xenocrysts not yield 980 Ma concordant dates? It may be noted (Fig. 5c, Zrn 7b.18; 6a, Zrn 7b. 25) that couple-of-microns wide protrusions continuous with texturally younger mantles cut across the older oscillatory

zoned cores in zircons. Reaction fronts may develop instabilities resulting in distinct protrusions and irregular reaction front geometries (e.g., Koehn et al., 2022 and references therein). Along such "reaction fingers or veins" conceivably melts may have permeated the older cores thus modifying the pristine isotopic signatures vis-a-vis the concordant age of the oscillatory zoned zircon cores (Fig. 13b, stage 1). The segregation of younger dates in the late-stage residual ferrodiorite melt relative to the BZGs seems to suggest that melt-mediated influence of isotope signatures from the 980 Ma zircon xenocrysts was variable within the intrusives in line with heterogeneous melt-zircon ratios as discussed above.

In contrast to the oscillatory zoned cores of BZG zircons and xenocryst cores in the sheared ferrodiorite vein, the large "cauliflower" zircons exhibit signatures of significant crystal plasticity such as continuous lattice bending, presence of dislocation arrays and subgrains, both with a clear relationship to the systematic lattice distortions (Fig. 9). At the same time, their ages are highly variable and there is a lack of consistent younging of ages towards the edge of the grains, while some irregular shaped grains (Fig. 9a) show clearly a higher degree of lattice distortion towards edges and protrusions. This spatially well defined, increased distortion is typical for stress induced lattice distortion in area of high strain, i.e., shear zones (e.g. Reddy et al. 2007; Piazolo et al. 2012) and is expected to be most significant in large grains as dislocation creep is favoured by large grain sizes. The highly irregular age distribution is therefore interpreted to be a combined effect of melt-mediated replacement reactions replacing pre-existing zircons and, at a late stage, forming the thin and assymmetric mantles, as well as enhanced pipe diffusion along subgrain boundaries and dislocation arrays which enhances elemental mobility (e.g., Piazolo et al. 2016). The latter is supported by the clear spatial correlation between lattice distortion and CL signatures related directly to subtle but important elemental variations.

Krause et al. (2001) assumed the oscillatory zoned cores to be typical of magmatic crystallization, and hence adopted the upper intercept to correspond to the emplacement age of the pluton. Based on phase equilibrium calculation, Nasipuri et al (2011) demonstrated that closed system crystallization of anorthosite from mantle-derived high-Al gabbro melts (cf. Fram and Longhi, 1992) cannot lead to the high Zr abundances measured in the Balangir ferrodiorites. Crustal contamination (open system) is necessary to explain Zr abundances in ferrodiorites. This can be achieved in two ways. First, the high-Al gabbro parental melts to anorthosite-leuconorite can be crustally contaminated. Or the residual melts of anorthosite-leuconorite crystallization need to be contaminated by crustal melts. In either case, zircon

xenocrysts from the crustally derived melts can be entrained within the ferrodiorites (Fig. 13a, c).

The multi-disciplinary approach adopted in this study zircon does not contradict the magmatic nature of the oscillatory zoned cores, but the available evidence does not support the ~980 Ma upper intercept age to correspond with the emplacement age of the pluton and the bordering intrusives. We suggest that the upper intercept date of ~980 Ma corresponds to the age of zircon xenocrysts inherited from the early Neoproterozoic ultra-high T basement gneisses from which the BZGs were derived by partial melting (Fig. 13a). These BZG melts contaminated the magma parental to the anorthite-leuconorite-ferrodiorite suite. Instead, we suggest the emplacement of the Balangir massif with the bordering ferrodiorites and the BZGs occurred at ~495 Ma, i.e. the lower intercept age of the discordia lines. It follows that the syn-emplacement high-T deformation-metamorphism (Dobmeier, 2006; Nasipuri and Bhattacharya, 2007; Nasipuri et al., 2011; Vadlamani, 2019) affecting the intrusives were Cambrian in age. An alternate scenario could be that the anorthosite pluton and BZGs were emplaced at ~980 Ma, and the zircons in the ferrodiorite dyke with the youngest discordant dates at ~495 Ma were modified by melt-mediated processes. This would however require the crust to remain hot at T > 700°C for ~ 600 million years. The supposition appears unrealistic.

5.6 Implication for the age of the collision between the Eastern Ghats Province and the Bastar Craton

There is a general consensus that the 1.1–0.9 Ga Rayner Complex (East Antarctica) and the 1.1–0.9 Ga Eastern Ghats Province (EGP; Rickers et al., 2001) in the SE coast of India were parts of a coherently evolved crustal domain in the Rodinia supercontinent (Mezger and Cosca, 1999; Simmat and Raith, 2008; Halpin et al., 2012; Morrissey et al., 2015). It is unclear however as to when the Rayner Complex-EGP composite welded with the Great India Landmass, and subsequently when did it split into EGP and Rayner complex. An alternative view is that the EGP split from the Rayner Complex and then welded with the Indian landmass; evidence for either event, at present, is unknown (Nasipuri et al., 2018).

One clue is provided by the available structural work which suggests that the EGP granulites, EGP-Rayner Complex composite, were thrust over the cratonic footwall (Gupta et al., 2000; Biswal and Sinha, 2003; Biswal et al., 2004, 2007; Das et al., 2008) formed by the Archean Bastar craton in the Great India Landmass (Fig. 1a, b; Mezger and Cosca, 1999; Boger et al., 2001; Morrissey et al., 2015; Biswal et al., 2004, 2007; Nasipuri et al., 2018; Padmaja et al., 2022).

The timing of this collision is controversial. One set of studies suggests that the collision occurred in the early Neoproterozoic (1.0–0.9 Ga; Padmaja et al., 2022 and references therein); these authors attribute the younger 0.6–0.5 Ga dates to tectonic reworking or reactivation without explicitly documenting the process that demonstrably stabilises the metamorphic mineral assemblages at amphibolite-granulite facies conditions. Another set of studies argue the collision occurred in the late Neoproterozoic/Cambrian (0.6–0.5 Ga; Biswal et al., 2004, 2007; Nasipuri et al., 2018) as part of the ca. 0.5 Ga assembly of the East Gondwanaland. These authors base their arguments on structurally-constrained petrological and chronological evidence from the cratonic footwall along the W/WNW-vergent interface between the Bastar craton and the EGP (Fig. 1a, b). In the Bastar Craton, the early Neoproterozoic dates (1.1–0.9 Ga) are lacking (Nasipuri et al., 2018; Biswal et al., 2007). In the Ranmal migmatite complex in the craton, syn-collisional anatexites (Das et al., 2008) are Cambrian (Nasipuri et al., 2008). Biswal et al. (2007) infers a late Neoproterozoic/Cambrian age for the collision-related transpressional shear zone with down dip stretching lineation in the ~1.6 Ga Khariar syenite (Biswal et al., 2004) within the Bastar Craton. The lack of 1.1–0.9 Ga dates from the cratonic footwall is considered compelling evidence favouring Cambrian collision, rather than a Rodinia age collision, between the EGP and the Bastar Craton. By contrast, both sets of dates, i.e., early Neoproterozoic (1.1–0.9 Ga) as well as late Neoproterozoic/Cambrian (0.6–0.5 Ga), are common in the hanging wall granulites along the western, north-western and the northern margins of the EGP.

For the Balangir pluton, close to the craton-EGP contact (Fig. 1), the upper intercept dates obtained in this study (~980 Ma) are interpreted to be the age of early Neoproterozoic zircon xenocrysts in the ultra-high T basement gneisses inherited by the BZGs and the ferrodiorite dyke. The lower intercept age (~495 Ma) of melt-mediated growth of zircon mantles around the ~980 Ma oscillatory-zoned inherited cores and the cauliflower-shaped zircons is inferred to be the age of emplacement of the BZGs and the ferrodiorite dyke that formed contemporaneously with, and causally related to, the emplacement of the Balangir anorthosite pluton. The Cambrian age obtained in this study closely corresponds with the U-Pb (titanite) metamorphic age (500 Ma) in calc-silicate gneisses at the margin of the Balangir pluton (Krause et al., 2001), and the Sm-Nd age (~499 Ma) obtained from the two 2-point isochrons (garnet-ferrodiorite and garnet-anorthosite) by Vadlamani (2019). It stands to reason that granulite facies metamorphism (Fig. 10a, b) manifested by the decomposition of garnet to pyroxene-plagioclase aggregates in BZGs (Fig. 4a, c) and the growth of garnet corona at the expense of plagioclase-pyroxene aggregates bordering plagioclase in ferrodiorites (Fig. 2c;

Bhattacharya et al., 2021) and along the interface between ferrodiorite dyke and anorthosite (Nasipuri et al., 2011) is a subsequent high-T deformation-metamorphic part of the Cambrian tectonism. Thus, the Cambrian age reported from the Eastern Ghats Province is not tectonic reworking but a major orogeny overprinting the early Neoproterozoic ultra-high T metamorphism in the EGP. This regional scale Cambrian (~495 Ma) tectonism along the western margin of the EGP (this study) is coeval with the collision between EGP and the Archean Bastar craton to the west, as part of the assembly of the East Gondwanaland (Biswal et al., 2007; Nasipuri et al., 2018). In other words, the EGP did not weld with the Indian Landmass until the Cambrian.

6. CONCLUSIONS

Interpreting discordant U-Pb zircon dates in crustal domains that experienced multiple high-T events remains highly challenging. The problem stems from the complexities in zircon nucleation-growth and dissolution mechanisms induced by multiple processes involving lattice diffusion and aqueous fluid and/or silicate melt mediated modifications that affect element mobility and isotopic redistribution at high temperatures. In order to address these issues, we provide results of chemical characterization (BSE, CL and EPMA imaging), crystallographic characterization (EBSD studies) and LA-ICPMS U-Pb dating in zircons with complex internal structures. These are integrated with existing field relations and petrological information in a suite of well-constrained intrusive suite bordering the Balangir anorthosite-leuconorite pluton (eastern India) emplaced syn-tectonic with high-T granulite facies metamorphism.

In BZGs, zircons formed at 700–950 °C consist of (a) embayed magmatic cores with oscillatory zones in Y, and Hf, and (b) chemically-homogenous mantles – having idiomorphic faces – that truncate the oscillatory zones but are crystallographically continuous with the cores. In the closely associated sheared Fe-rich ferrodiorite dykes (crustally contaminated anorthosite residual melts) that truncate the margin-parallel foliation in the BZGs, coarse-grained, cauliflower-shaped zircons (formed at 700–750 °C) studded with micropores are associated with a subsidiary population of sub-idioblastic zircons inherited from BZGs. The cauliflower-shaped zircons formed by complete replacement of entrained zircon and growth upon these grains as the abundances of plagioclase incompatible elements (including Zr) increased in a decreasing proportion of fractionated residual ferrodiorite melts.

The U-Pb zircon dates in the intrusives, individually and collectively, constitute a near-unique discordia with the upper intercept at 968–1001 Ma (mean~980 Ma), and the

lower intercept at ~495 Ma. We infer that the upper intercept date corresponds to the age of zircon xenocrysts entrained within the intrusives from the protolith (basement gneisses). This was followed by a single stage melt-mediated age-modifying high-T tectono-metamorphic event that occurred at ~495 Ma. The discordance in U-Pb systematic was induced by high-T melt-mediated dissolution of ~980 Ma oscillatory zoned cores in zircon followed by precipitation of epitaxially grown mantles in the BZGs at the reaction interface and extensive replacement and growth of cauliflower-shaped zircons at ~495 Ma. All grains underwent a late-stage minor melt-mediated interface-coupled replacement reaction resulting in asymmetric mantles. The lack of concordant dates and the Pb loss along the discordia are attributed to the variable inheritance of isotopic signatures of the ~980 Ma zircon xenocrysts in the ~495 Ma zircons in response to the interface coupled dissolution-precipitation processes. The extent of measurable inheritance however is less pronounced in the large cauliflower-shaped magmatic zircons in the sheared ferrodiorite dykes as these zircons were additionally subject to significant crystal plastic deformation resulting in crystal lattice bending and dislocation arrays facililtating fast pipe diffusion and therefore ages closer to the age of deformation.

The ~495 Ma tectonic event in the Eastern Ghats Province involved anorthosite pluton emplacement and granulite facies deformation-metamorphism. This event at ~495 Ma is correlated with the collision between the Rodinia-age (~980 Ma) Eastern Ghats Province and the Archean cratonic nucleus of India.

ACKNOWLEDGEMENTS

The authors acknowledge in-depth discussions with Prof. Nathan Daczko (Macquarie University) regarding the potential effect of fluid mediated replacement reactions on the age signatures of zircon in general. Anwesa acknowledges the postdoctoral research fellowship provided to her by the Indian Institute of Technology Bombay during the course of this work. The authors acknowledge the thought-provoking and detailed comments provided by an anonymous journal reviewer and Fernando Corfu. Their comments helped improving this study. We thank the efficient Editorial handling of the manuscript by Claudia Romano.

REFERENCES

Aftalion, M., Bowes, D. R., Dash, B., Dempster, T. J., 1988. Late Proterozoic charnockites of Orissa, India: A U-Pb and Rb-Sr isotopic study. The Journal of Geology 96, 663–676. https://doi.org/10.1086/629269

Banerjee, A., Sequeira, N., Cogné, N., Prabhakar, N., Bhattacharya, A., 2022a. Early Neoproterozoic tectonics in the Godhra–Chhota Udepur sector: Evidence for two-stage accretion in the Great Indian Proterozoic Fold Belt. Lithosphere 8. https://doi.org/10.2113/2022/9322892.

Banerjee, A., Cogné, N., Sequeira, N., Bhattacharya, A., 2022b. Dynamics of early Neoproterozoic accretion, west-central India: I: Geochronology and Geochemistry: Lithos 422-423. https://doi.org/10.1016/j.lithos.2022.106715

Bernard-Griffiths, J., Peucat, J.J., Ménot, R.P., 1991. Isotopic (Rb□ Sr, U□ Pb and Sm□ Nd) and trace element geochemistry of eclogites from the pan-African Belt: A case study of REE fractionation during high-grade metamorphism. Lithos 27, 43–57. https://doi.org/10.1016/0024-4937(91)90019-H

Bhadra. S., Das, S., Bhattacharya, A., 2007. Shear zone-hosted migmatites (Eastern India): the role of dynamic melting in the generation of REE-depleted felsic melts, and implications for disequilibrium melting. Journal of Petrology 48, 435–457. https://doi.org/10.1093/petrology/egl066

Bhattacharya, A., Raith, M., Hoernes, S., Banerjee, D., 1988. Geochemical evolution of the massif-type anorthosite complex at Bolangir in the Eastern Ghats Belt of India. Journal of Petrology 39, 1169–1195. https://doi.org/10.1093/petroj/39.6.1169

Bhattacharya, A., Dey, J., Kushwaha, A., Sequeira, N., 2021. Growth of Coronal Garnet in Anhydrous High-Fe Ultrabasic Rocks: The Interplay Between Metamorphic Reaction Progress, Local Strain Heterogeneity and Grain Boundary Diffusion. Journal of Petrology 62. https://doi.org/10.1093/petrology/egab067

Biswal, T. K., Sinha, S., 2003. Deformation history of the NW salient of the Eastern Ghats Mobile Belt, India. Journal of Asian Earth Sciences 22, 157–169. https://doi.org/10.1016/S1367-9120(02)00182-7

Biswal, T. K., Ahuja, H., Sahu, H. S., 2004. Emplacement kinematics of nepheline syenites from the Terrane Boundary Shear Zone of the East-ern Ghats Mobile Belt, west of Khariar, NW Orissa: Evidence from meso- and microstructures. Journal of Earth System Science 113, 785–793. https://doi.org/10.1007/BF02704037

Biswal, T. K., De Waale, B., Ahuja, H., 2007. Timing and dynamics of the juxtaposition of the Eastern Ghats Mobile Belt against the Bhandara Craton, India: A structural and zircon U-Pb SHRIMP study of the fold-thrust belt and associated nepheline syenite plutons. Tectonics T26, TC4006. https://doi.org/10.1029/2006TC002005

Bloch, E. M., Jollands, M. C., Tollan, P., Plane, F., Bouvier, A-S., Hervig. R., Berry, A. J., Zaubitzer, C., Escrig, S., Muntener, O., Ilbanez-Mejia, M., Alleon, J., Meibom, A., Baumgartner, L. P., Marin-Carbone, J., Newville, M., 2022. Diffusion anisotropy of Ti in zircon and implications for Ti-in-zircon thermometry. Earth and Planetary Science Letters 578, 117317. https://doi.org/10.1016/j.epsl.2021.117317

Bogdanova, S. V., Belousova, E., De Waele, B., Larionov, A. N., Piazolo, S., Postnikov, A. V., & Samsonov, A. V., 2021. Palaeoproterozoic reworking of early Archaean lithospheric blocks: Rocks and zircon records from charnockitoids in Volgo-Uralia. Precambrian Research 360, 106224. https://doi.org/10.1016/j.precamres.2021.106224

Boger, S. D., Wilson, C. J. L., Fanning, C. M., 2001. Early Paleozoic tectonism within the East Antarctic craton: The final suture between east and west Gondwana? Geology 29, 463–466. https://doi.org/10.1130/0091-7613(2001)029<0463:EPTWTE>2.0.CO;2

Braun, J, van der Beek, P., Batt, G., 2006. Basics of thermochronology: from *t-T* paths to ages, In: Quantitative thermochronology: Numerical methods for the interpretation of thermochronological data. Cambridge University Press, Cambridge. 24–27p.

Chen, W., Xiong, X., Takahashi, E., 2021. Zircon solubility in solute-rich supercritical fluids and Zr transfer from slab to wedge in the deep subduction process. Journal of Geophysical Research: Solid Earth 126, e2021JB021970. https://doi. org/10.1029/2021JB021970

Chew, D.M., Petrus, J.A., Kenny, G.G., McEvoy, N., 2017. Rapid high-resolution U-Pb LA Q-ICPMS age mapping of zircon. Journal of Analytical Atomic. Spectrometry 32, 262–276. https://doi.org/10.1039/c6ja00404k.

Chew, D., Drost, K., Marsh, J. H., Petrus, J. A., 2021. LA-ICP-MS imaging in the geosciences and its applications to geochronology. Chemical Geology 559, 119917 https://doi.org/10.1016/j.chemgeo.2020.119917

Cherniak, D. J., Watson, E. B., 2001. Pb diffusion in zircon. Chemical Geology 172, 5–24. https://doi.org/10.1016/S0009-2541(00)00233-3

Cherniak, D. J., Watson, E. B., 2003. Diffusion in zircon. Reviews in Mineralogy and Geochemistry 53, 113–143. https://doi.org/10.2113/0530113

Cherniak, D. J., Watson, E. B., 2006. Ti diffusion in zircon. In: *AGU Fall Meeting Abstracts* 2006, V31F-02.

Cherniak, D. J., Lanford, W. A., Ryerson, F. J., 1991. Lead diffusion in apatite and zircon using ion implantation and Rutherford Backscattering techniques. Geochimica Cosmochimica. Acta 55, 1663–1673. https://doi.org/10.1016/0016-7037(91)90137-T

Cherniak, D. J., Hanchar, J. M., Watson, E. B., 1997a. Rare-Earth diffusion in zircon. Chemical Geology 134, 289–301. https://doi.org/10.1016/S0009-2541(96)00098-8

Cherniak, D. J., Hanchar, J. M., Watson, E. B., 1997b. Diffusion of tetravalent cations in zircon. Contribution Mineralogy Petrology 127, 383–390. https://doi.org/10.1007/s004100050287

Connelly, J. N., 2001. Degree of preservation of igneous zonation in zircon as a signpost for concordancy in U/Pb geochronology. Chemical Geology 172, 25–39. https://doi.org/10.1016/S0009-2541(00)00234-5

Corfu, F., Hanchar, J. M., Hoskin, P. W. O., Kinny, P., 2003. Atlas of zircon textures. In: Reviews in Mineralogy and Geochemistry 53, 469–500. https://doi.org/10.2113/0530469

Corvò, S., Maino, M., Piazolo, S., Kylander-Clark, A. R., Orlando, A., Seno, S., Langone, A., 2023. Crystal plasticity and fluid availability govern the ability of titanite to record the age of deformation. Earth and Planetary Science Letters 620, 118349. https://doi.org/10.1016/j.epsl.2023.118349

Das, S., Nasipuri, P., Bhattacharya, A., Swaminathan, S., 2008. The thrust-contact between the Eastern Ghats Belt and the adjoining Bastar craton (Eastern India): Evidence from mafic granulites and tectonic implications. Precambrian Research 162, 70–85. https://doi.org/10.1016/j.precamres.2007.07.013

Dobmeier, C., 2006. Emplacement of Proterozoic massif-type anorthosite during regional shortening: evidence from the Bolangir anorthosite complex (Eastern Ghats Province, India). International Journal of Earth Science 95, 543–555. https://doi.org/10.1007/s00531-005-0050-x

Ferry, J. M., Watson, E. B., 2007. New thermodynamic models and revised calibrations for the Ti-in-zircon and Zr-in-rutile thermometers. Contributions to Mineralogy and Petrology 154, 429–437. https://doi.org/10.1007/s00410-007-0201-0

Flowers, R. M., Bowring, S. A., Williams, M. L., 2006. Timescales and significance of high-pressure, high-temperature metamorphism and mafic dike anatexis, Snowbird tectonic zone, Canada. Contribution Mineralogy Petrology 151, 558–581. https://doi.org/10.1007/s00410-006-0066-7

Flowers, R. M., Schmitt, A. K., Frove, M., 2010. Decoupling of U–Pb dates from chemical and crystallographic domains in granulite facies zircon. Chemical Geology 270, 20–30. https://doi.org/10.1016/j.chemgeo.2009.11.002

Fougerouse, T. G., Reddy, S. M., Aleshin, M., Martin, L., Doucet, L. S., Quadir, Z., Rickard, D. S. W., 2024. Melt-mediated re-equilibration of zircon produced during meltdown of the Chernobyl reactor. American Mineralogist 109, 8–14. https://doi.org/10.2138/am-2022-8824

Fram, M. S., Longhi, J., 1992. Phase equilibria of dikes associated with Proterozoic anorthosite complexes. American Mineralogist 77**,** 113–132**.**

Fu, B., Paul, B., Cliff, J., Bröcker, M. and Bulle, F., 2012. O-Hf isotope constraints on the origin of zircon in high-pressure mélange blocks and associated matrix rocks from Tinos and Syros, Greece. European Journal of Mineralogy 24, 277. https://doi.org/10.1127/0935-1221/2011/0023-2131

Gagnevin, D., Daly, J. S., Kronz, A., 2010. Zircon texture and chemical composition as a guide to magmatic processes and mixing in a granitic environment and coeval volcanic system. Contributions to Mineralogy Petrology 159, 579–596. https://doi.org/10.1007/s00410-009-0443-0

Ge, R., Wilde, S. A., Nemchin, A.A., Whitehouse, M.J., Bellucci, J. J., Erickson, T. M., 2019. Mechanisms and consequences of intra-crystalline enrichment of ancient radiogenic Pb in detrital Hadean zircons from the Jack Hills, Western Australia. Earth and Planetary Science Letters 517, 38–49. https://doi.org/10.1016/j.epsl.2019.04.005

Gupta, S., Bhattacharya, A., Raith, M., Nanda, J. K., 2000. Contrasting pressure–temperature–deformation history across a vestigial craton–mobile belt boundary: the western margin of the Eastern Ghats Belt at Deobhog, India. Journal of Metamorphic Geology 18, 683–697. https://doi.org/10.1046/j.1525-1314.2000.00288.x

Halpin, J. A., Daczko, N. R., Milan, L. A., Clarke, G. L., 2012. Decoding near-concordant U–Pb zircon ages spanning several hundred million years: recrystallisation, metamictisation or diffusion? Contributions to Mineralogy and Petrology 163, 67–85. https://doi.org/10.1007/s00410-011-0659-7

Hanchar, J. M., Miller, C. F. 1993. Zircon zonation patterns as revealed by cathode luminescence and back scattered electron images: Implications for interpretation of complex crustal histories. Chemical Geology 110, 1–13. https://doi.org/10.1016/0009-2541(93)90244-D

Harrison, T. M., Watson, E.B., 1983a. Kinetics of zircon dissolution and zirconium diffusion in granitic melts of variable water content. Contributions to Mineralogy and Petrology 84, 66–72. https://doi.org/10.1007/BF01132331

Harrison, T. M., Watson, E. B., 1983b. Zircon saturation revisited' temperature and composition effects in a variety of crustal magma types. Earth and Planetary Science Letters, 64, 295–304. https://doi.org/10.1016/0012-821X(83)90211-X

Harrison, T. M., Watson, E. B., Aikman, A. B., 2007. Temperature spectra of zircon crystallization in plutonic rocks. Geology 35, 635–638. https://doi.org/10.1130/G23505A.1

Holycross, M.E., Watson, E.B., 2018. Trace element diffusion and kinetic fractionation in wet rhyolitic melt. Geochimica et Cosmochimica Acta 232, 14–29. https://doi.org/10.1016/j.gca.2018.04.006

Horstwood, M. S. A., Košler, J., Gehrels, G., Jackson, S. E., McLean, N. M., Paton, C., Pearson, N.J., Sircombe, K., Sylvester, P., Vermeesch, P., Bowring, J. F., Condon, D.J., Schoene, B., 2016. Community-Derived Standards for LA-ICP-MS U-(Th-)Pb Geochronology – Uncertainty Propagation, Age Interpretation and Data Reporting. Geostandards and Geoanalytical Research 40, 311–332. https://doi.org/10.1111/j.1751- 908X.2016.00379.x

Huijsmans, J. R., Hamers, M., Drury, M. R., Lee, J. K. W., 2022. Recrystallisation and trace-element mobility in zircons: Implications for U-Pb dating. Minerals 12, 1489. https://doi.org/10.3390/min12121489

Kelly, C. J., Schneider, D. A., Jackson, S. E., Kalbfleisch, T., McFarlane, C. R., 2017. Insights into low- to moderate-temperature recrystallization of zircon: Unpolished crystal depth profile techniques and geochemical mapping. Chemical Geology 449, 82–98. https://doi.org/10.1016/j.chemgeo.2016.11.035

Koehn, D., Piazolo, S., Beaudoin, N.E., Kelka, U., Spruženiece, L., Putnis, C.V., Toussaint, R., 2021. Relative rates of fluid advection, elemental diffusion and replacement govern reaction front patterns. Earth and Planetary Science Letters 565, 116950. https://doi.org/10.1016/j.epsl.2021.116950

Krause, O., Dobmeier, C., Raith, M. M., Mezger, K., 2001. Age of emplacement of massif-type anorthosites in the Eastern Ghats Belt, India: constraints from U–Pb zircon dating and structural studies. Precambrian Research 109, 25–38. https://doi.org/10.1016/S0301-9268(01)00140-1

Kunz, B. E., Regis, D., Engi, M., 2018. Zircon ages in granulite facies rocks: decoupling from geochemistry above 850 °C? Contributions to Mineralogy and Petrology 173, 26. https://doi.org/10.1007/s00410-018-1454-5

Langone, A., José, A. P-N, Ji, W-Q., Zanetti, A., Mazzucchelli, M., Tiepolo, M., Giovanardi, T., Bonazzi, M., 2017. Ductile–brittle deformation effects on crystal-chemistry and U–Pb ages of magmatic and metasomatic zircons from a dyke of the Finero Mafic Complex (Ivrea–Verbano Zone, Italian Alps). Lithos 284-285, 493–511. https://doi.org/10.1016/j.lithos.2017.04.020

Langone, A., Zanetti, A., Daczko, N. R., Piazolo, S., Tiepolo, M., Mazzucchelli, M., 2018. Zircon U-Pb Dating of a Lower Crustal Shear Zone: A Case Study from the Northern Sector of the Ivrea-Verbano Zone (Val Cannobina, Italy). Tectonics 37, 322–342. https://doi.org/10.1002/2017TC004638

Lee, J. K. W., William, I. S., Ellis, D. J., 1997. Pb, U and Th diffusion in natural zircon. Nature 390, 159–161. https://doi.org/10.1038/36554

Marsellos, A. E., Garver, J. I., 2010. Radiation damage and uranium concentration in zircon as assessed by Raman spectroscopy and neutron irradiation. American Mineralogist 95, 1192–120. https://doi.org/10.2138/am.2010.3264

McFarlane, C. R. M., Connelly, J. N. Connelly, Carlson, W. D., 2005. Intracrystalline redistribution of Pb in zircon during high-temperature contact metamorphism. Chemical Geology 217, 1–28. https://doi.org/10.1016/j.chemgeo.2004.11.019

Meldrum, A., Boatner, L. A., Weber, W. J., Ewing, R.C., 1998. Radiation damage in zircon and monazite. Geochimica et Cosmochimica Acta 62, 2509–2520. https://doi.org/10.1016/S0016-7037(98)00174-4

Menegon, L., Nasipuri, P., Stünitz, H., Behrens, H., Ravna, E., 2011. Dry and strong quartz during deformation of the lower crust in the presence of melt. Journal of Geophysical Research: Solid Earth 116, B10410. https://doi.org/10.1029/2011JB008371

Mezger, K., Cosca, M.A., 1999. The thermal history of the Eastern Ghats Belt (India) as revealed by U–Pb and 40Ar/39Ar dating of metamorphic and magmatic minerals: Implications for the SWEAT correlation. Precambrian Research 94, 251–271. https://doi.org/10.1016/S0301-9268(98)00118-1

Mitchell, R. J., Johnson, T. E., Clarke, C., Gupta, S., Brown, M., Harley, S. L., Taylor, R., 2019. Neoproterozoic evolution and Cambrian reworking of ultrahigh temperature granulites in the Eastern Ghats Province, India. Journal of Metamorphic Geology 37, 977–1006. https://doi.org/10.1111/jmg.12451

Morrissey, L. J., Hand, M., Kelsey, D. E., 2015. Multi-stage metamorphism in the Rayner–Eastern Ghats Terrane: P–T–t constraints from the northern Prince Charles Mountains, east Antarctica. Precambrian Research 267, 137–163. https://doi.org/10.1016/j.precamres.2015.06.003

Moser, D. E., Davis, W. J., Reddy, S. M., Flemni, R. L., Hart, R. J., 2009. Zircon U–Pb strain chronometry reveals deep impact-triggered flow. Earth and Planetary Science Letters 277, 73–79. https://doi.org/10.1016/j.epsl.2008.09.036

Mukherjee, A., 1989. *P-T*-time history and thermal modelling of an anorthosite-granulite interface, Eastern Ghats metamorphic belt, India. In: Daly J. S., Cliff, R. A., Yardley, B.W. (Eds.) Evolution of Metamorphic Belts. Geological Society of London Special Publications 43, 265–274. https://doi.org/10.1144/GSL.SP.1989.043.01.18

Mukherjee, A., Bhattacharya, A., Chakraborty, S. C., 1986. Convergent phase equilibria at the massif anorthosite-granulite interface near Bolangir, Orissa, India, and the thermal evolution of a part of the Indian Shield. Precambrian Research 34, 69–104. https://doi.org/10.1016/0301-9268(86)90060-4

Mukherjee, A. K., Bhattacharya, A., 1997. Tectonothermal evolution of the gneiss complex at Salur in the Eastern Ghats Grnaulite Belt of India. Journal of Metamorphic Geology 15, 719–734. https://doi.org/10.1111/j.1525-1314.1997.00051.x

Murakami, T., Chakoumakos, B.C., Ewing, R.C., Lumpkin, G.R., Weber, W.J., 1991. Alpha-decay event damage in zircon. American Mineralogist 76, 1510–1532.

Nasdala, L., Pidgeon, R. T., Wolf, D., Irmer, G., 1998. Metamictization and U-Pb isotopic discordance in single zircons: A combined Raman microprobe and SHRIMP ion probe study. Mineralogy and Petrology 62, 1–27. https://doi.org/10.1007/BF01173760

Nasipuri, P., Bhadra, S., 2013. Structural framework for the emplacement of the Bolangir anorthosite massif in the Eastern Ghats Granulite Belt, India: implications for post-Rodinia pre-Gondwana tectonics. Mineralogy and Petrology 107, 861–880. https://doi.org/10.1007/s00710-013-0281-7

Nasipuri, P., Bhattacharya, A., 2007. Melt-assisted interior to margin switch from dislocation to diffusion creep in coarse grained plagioclase: Evidence from a deformed anorthosite pluton. Journal of Structural Geology 29, 1327–1338. https://doi.org/10.1016/j.jsg.2007.04.005

Nasipuri, P, Bhattacharya, A., Das, S., 2008. Metamorphic reactions in dry and aluminous granulites: A Perple_X P – T pseudosection analysis of the influence of effective

reaction volume. Contributions to Mineralogy and Petrology 157, 301–311. https://doi.org/10.1007/s00410-008-0335-8

Nasipuri, P., Bhattacharya, A., Satyanarayan, M., 2011. Localized pluton deformation and linked focused flow of low-volume fraction residual melt in deforming plagioclase cumulates. Bulletin of the Geological Society of America 123, 669–680. https://doi.org/10.1130/B26408.1

Nasipuri, P., Corfu, F., Bhattacharya, A., 2018. Eastern Ghats Province (India)–Rayner Complex (Antarctica) accretion: Timing the event. Lithosphere 10, 523–529. https://doi.org/10.1130/L703.1

Padmaja, J., Sarkar, T., Sorcar, N., Mukherjee, S., Das, N., and Dasgupta, S., 2022. Petrochronological evolution of Mg-Al granulites and associated metapelites from the contact zone of the Archean Bastar Craton and Proterozoic Eastern Ghats Province, and its implications: Geosystems and Geoenvironment 1, 100041. https://doi.org/10.1016/j.geogeo.2022.100041

Peterman, E. M., Grove, M., 2010. Growth conditions of symplectic muscovite + quartz: Implications for quantifying retrograde metamorphism in exhumed magmatic arcs. Geology 38, 1071–1074. https://doi.org/10.1130/G31449.1

Peterman, E. M, Reddy, S. M., Saxey, D. W., Snoeyenbos, D. R., Rickard, W. D. A., Fougerouse, D., Kylander-Clark, A. R. C., 2016. Nanogeochronology of discordant zircon measured by atom probe microscopy of Pb-enriched dislocation loops. Science Advances 2, e1601318. https://doi.org/10.1126/sciadv.1601318

Peucat, J. J., Bernard-Griffiths, J., Gil Ibarguchi, J-I., Dallmeyer, R. D., Menot, R. P., Cornichet, J., Iglesias Ponce de Leon, M., 1990. Geochemical and geochronological cross section of the deep Variscan crust: The Cabo Ortega! High-pressure nappe (northwestern Spain). Tectonophysics 177, 263–292. https://doi.org/10.1016/0040-1951(90)90285-G

Piazolo, S., Austrheim, H., Whitehouse, M., 2012. Brittle-ductile microfabrics in naturally deformed zircon: Deformation mechanisms and consequences for U-Pb dating. American Mineralogist 97, 1544–1563. https://doi.org/10.2138/am.2012.3966

Piazolo, S., La Fontaine, A., Trimby, P., Harley, S., Yang, L., Armstrong, R., Cairney, J. M., 2016. Deformation induced trace element redistribution in zircon revealed using atom probe tomography. Nature Communications 7, 10490. https://doi.org/10.1038/ncomms10490

Pidgeon, R. T., 1992. Recrystallization of oscillatory zoned zircons: Some chronological and petrological implications. Contribution to Mineralogy and Petrology 110, 463–472. https://doi.org/10.1007/BF00344081

Poulaki, E. M., Stockli, D. F., Flansburg, M. E., Gevedon, M. L., Stockli, L-D., Barnes, J. D., Soukis, K., Kitajima, K., Valley, J. W., 2021. Zircon U-Pb and geochemical signatures in high-pressure, low-temperature metamorphic rocks as recorders of subduction zone processes, Sikinos and Ios islands, Greece. Chemical Geology 582, 120447. https://doi.org/10.1016/j.chemgeo.2021.120447

Prasad, S., Bhattacharya, A., Raith, M. M., Bhadra, S., 2005. The origin of orthopyroxene/biotite + plagioclase coronas from the Bolangir anorthosite complex (India), and implications for reconstructing P-T paths. American Mineralogist 90, 291–303. https://doi.org/10.2138/am.2005.1487

Putnis, A., 2009. Mineral replacement reactions. Reviews in Mineralogy and Geochemistry 70, 87–124. https://doi.org/10.2138/rmg.2009.70.3

Pystina, Y., Pystin. A., 2019. Th/U relations as an indicator of the genesis of metamorphic zircons (on the example of the north of the Urals). In: 14th International Congress for Applied Mineralogy (ICAM2019) Belgorod State Technological University named after VG Shukhov, 23–27 September 2019, Belgorod, Russia 14, 129–132. Springer International Publishing. https://doi.org/10.1007/978-3-030-22974-0_30

Raith, M., Bhattacharya, A., Horenes, S. 1997. A HFSE-and REE-enriched ferrodiorite suite from the Bolangir anorthosite complex, Eastern Ghats Belt, India. Proceedings of the Indian Academy of Sciences (Earth and Planetary Sciences) 106, 299–311. https://doi.org/10.1007/BF02843455

Raith, M. M., Mahapatro, S, N., Upadhyay, D., Berndt, J., Mezger, K., Nanda, J. K., 2014. Age and P–T evolution of the Neoproterozoic Turkel Anorthosite Complex, Eastern Ghats Province, India. Precambrian Research 254, 87–113. https://doi.org/10.1016/j.precamres.2014.08.003

Reddy, S. M., Timms, N. E., Pantleon, W., Trimby, P., 2007. Quantitative characterization of plastic deformation of zircon and geological implications. Contributions to Mineralogy and Petrology 153, 625–645. https://doi.org/10.1007/s00410-006-0174-4

Rickers, K., Mezger, K., Raith M. M., 2001. Evolution of the continental crust in the Proterozoic Eastern Ghats Belt, India and new constraints for Rodinia reconstruction: implications from Sm–Nd, Rb–Sr and Pb–Pb isotopes. Precambrian Research 112, 183–210. https://doi.org/10.1016/S0301-9268(01)00146-2

Rimsa, A., Whitehouse, M. J., Johansson, L., Piazolo, S., 2007. Brittle fracturing and fracture healing of zircon: An integrated cathodoluminescence, EBSD, U-Th-Pb, and REE study. American Mineralogist 92, 1213–1224. https://doi.org/10.2138/am.2007.2458

Simmat, R., Raith, M. M., 2008. U–Th–Pb monazite geochronometry of the Eastern Ghats Belt, India: Timing and spatial disposition of poly-metamorphism. Precambrian Research 162, 16–39. https://doi.org/10.1016/j.precamres.2007.07.016

Spruzeniece, L., Piazolo, S., Maynard-Casely, H. E., 2017. Deformation-resembling microstructure created by fluid-mediated dissolution–precipitation reactions. Nature Communicatons 8, 14032. https://doi.org/10.1038/ncomms14032

Tak, M. W., Mitra, D., Chatterjee, P. K., 1966. A note on the occurrence of anorthosite in the Bolangir-Patna district, Orissa. Indian Minerals 20, 339–342.

Timms, N. E., Kinny, P. D., Reddy, S. M., 2006. Enhanced diffusion of Uranium and Thorium linked to crystal plasticity in zircon. Geochemical Transactions **7,** 10. https://doi.org/10.1186/1467-4866-7-10

Tretiakova, I. G., Belousova, E. A., Malkovets, V. G., Griffin, W. L., Piazolo, S., Pearson, N. J., O'Reilly, S., Nishido, H., 2016. Recurrent magmatic activity on a lithosphere-scale structure: Crystallization and deformation in kimberlitic zircons. Gondwana Research 42, 126–132. https://doi.org/10.1016/j.gr.2016.10.006

Vadlamani, R., 2019. Cambrian Garnet Sm-Nd Isotopic Ages from the polydeformed Bolangir Anorthosite Complex, Eastern Ghats Belt, India: Implications for intraplate Orogeny Coeval with Kuunga Orogeny during Gondwana Assembly. Journal of Geology 127, 437–456. https://doi.org/10.1086/703463

Van Gosen, B.S., Verplanck, P.L., Seal, R.R., II, Long, K.R., and Gambogi, Joseph, 2017. Rare-earth elements. In: Schulz, K.J., DeYoung, J.H., Jr., Seal, R.R., II, Bradley, D.C., (Eds.) Critical mineral resources of the United States – Economic and environmental geology and prospects for future supply: U.S. Geological Survey Professional Paper 1802, O1–O31. https://doi.org/10.3133/pp1802O.

Varga, J., Raimondo, T., Daczko, N. R., Adam, J., 2020. Experimental alteration of monazite in granitic melt: Variable U–Th–Pb and REE mobility during melt-mediated coupled dissolution-precipitation. Chemical Geology 544, 119602. https://doi.org/10.1016/j.chemgeo.2020.119602

Vermeesch, P., 2018. IsoplotR: A free and open toolbox for geochronology. Geoscience Frontiers 9, 1479-1493. https://doi.org/10.1016/j.gsf.2018.04.001

Vernon, R.H., Johnson, S.E., Melis, E.A., 2004. Emplacement-related microstructures in the margin of a deformed tonalite pluton: the San Jose´ pluton, Baja California, Mexico. Journal of Structural Geology 26, 1887–1884. https://doi.org/10.1016/j.jsg.2004.02.007

Vonlanthen, P., Fitz Gerald, J. D., Rubatto, D., Hermann, J., 2012. Recrystallization rims in zircon (Valle d'Arbedo, Switzerland): An integrated cathodoluminescence, LA-ICP-MS, SHRIMP, and TEM study. American Mineralogist 97, 369–377. https://doi.org/10.2138/am.2012.3854

Watson, E. B., Wark, D. A., Thomas, J. B., 2006. Crystallization thermometers for zircon and rutile. Contributions to Mineralogy and Petrology 151, 413–433. https://doi.org/10.1007/s00410-006-0068-5

Wayne, D. M., Sinha, A. K., 1988. Physical and chemical response of zircons to deformation. Contributions to Mineralogy Petrology 98, 109–121. https://doi.org/10.1007/BF00371915

Whitney, D.L. Evans, B.W., 2010. Abbreviations for names of rock-forming minerals. American Mineralogist, 95, 185–187. https://doi.org/10.2138/am.2010.3371

Williams, M.L., Hanmer, S., Kopf, C., Darrach, M., 1995. Syntectonic generation and segregation of tonalitic melts from amphibolite dikes in the lower crust, Striding-Athabasca mylonite zone, northern Saskatchewan. Journal of Geophysical Research: Solid Earth 100, 15717–15734. https://doi.org/10.1029/95JB00760

Woodhead, J.A., Rossman, G.R., Silver, L.T., 1991. The metamictization of zircon: Radiation dose-dependent structural characteristics. American Mineralogist 76, 74–82.

Zhang, Y., Ni, H., Chen, Y., 2010. Diffusion data in silicate melts. Reviews in Mineralogy and Geochemistry 72, 311–408.

FIGURE CAPTIONS

Fig. 1: (a) Generalised geological map showing the crustal domains in the Eastern Ghats granulite Belt. The locations of the Ranmal migmatite Complex (R) and the Khariar syenite complex (K) at the western margin of the Eastern Ghats Province are show as stars. (b) Tectonic map of the northern part of the 1.1–0.9 Ga Eastern Ghats Province showing the location of the Balangir anorthosite massif simplified after Raith et al (2014); (c) simplified lithologic-structural map of the Balangir anorthosite complex (simplified after Bhattacharya et al., 1998) showing the locations of the analyzed samples.

Fig. 2: Field photographs. (a) 3-dinensional view of south-dipping margin-parallel foliation MPF (cf. Vernon et al., 2004) in garnet-bearing BZGs defined by drawn out K-feldspar (best observed on top surface), plagioclase and pyroxene aggregates (see fig 3a for detailed view). (b) Margin-parallel foliation in anorthosite (leucocratic) defined by biotite ± orthopyroxene schlieren truncated by N-striking shear zone hosted ferrodiorite dyke BG-1B (melanocratic). Thin scale BSE image in Fig. 3b provides close up of the ferrodiorite dyke. Traces show the orientations of the margin-parallel foliation, MPF. In both (a) and (b), head of marker (15 cm long) points to the north. (c) In ferrodiorite parallel to the pluton margin, beads of coronal garnet inwards of the margins of recrystallized plagioclase clasts wrapped by pyroxene-ilmenite margin-parallel foliation aggregates shown by arrow. Coin diameter is 2cm.

Fig. 3: Compositional plots of intrusives in the Balangir anorthosite complex (based on data from Bhattacharya et al., 1998) showing chemical variation of selected major element oxides (molar proportion) and selected trace element abundances in anorthosite-leuconorite, BZGs and ferrodiorites (data from Bhattacharya et al, 1988). (a) Molar abundances of major element oxides. (b) Zr abundances in ferrodiorites and BZGs plotted against basicity (M) of felsic melts (Harrison and Watson, 1983). Note the Zr abundances and M vales of the Fe-rich ferrodiorites lie outside the range shown in Harrison and Watson (1983) shown by the grey box. (c, d) Zr vs Y and Zr vs Th in the rocks.

Fig. 4: Full thin-section BSE mosaic of (a) nature of margin-parallel foliation in BZG BG-6 and (b) N-striking ferrodiorite BG-1B. Red boxes show locations of zircon grains. The major minerals in the rock are labelled; abbreviations used are after Whitney and Evans, 2010. Traces show the orientations of the margin-parallel foliations. In (b) note the younger margin-parallel foliation (MPF) in anorthosite and the later ferrodiorite-hosted shear zone fabric. The bright layers (folded) within anorthosite are thin ferrodiorite residual melts. (c, d) are blown up images of blue boxes in (a) and (b) respectively.

Fig. 5: Cathodoluminescence (CL) and backscatter electron (BSE) images of representative zircon grains in BZGs BG-5, 6 and 7 (a-c), and in ferrodiorite dyke BG-1B (d) showing the morphological features and internal structures in the zircon crystals. ‘B’ are inscribed alongside the BSE images of the grains; the corresponding images are obtained using CL. White arrows in (a-c) indicate the sharp truncation fronts of the mantles, black arrows indicate mantles that protrude into the cores.

Fig. 6: BSE images with CL images in insets exhibits morphology and internal structures in zircons hosted within garnet (predates MPF, not shown) in BZG BG 7.

Fig. 7: X-ray element maps for Hf, U, and Y for zircon grains in two BZGs (BG 5, 6) and the ferrodiorite BG-1B. The left column are the CL images of the zircon grains. The red-shaded grain in the uranium scan of Zrn 1Bc.4 in BG-1B is K-feldspar.

Fig. 8: Crystallographic orientation relationships of zircon grains in the boundary granite, sample BG-5; (a) Zrn5a.5, (b) Zrn 5b.20. (a_i) CL image with 3D representation of crystal orientation and map of relative orientation change map with core marked; note oscillatory zoning coincides both with slight orientation changes and low index facets of crystal and slight gradual orientation change of whole grain; (a_{ii}) low angle rotation axes orientation in crystal coordinates for core and mantle; note axes are well defined for the core, while mantle shows similar general axes but less well defined; (a_{iii}) Pole figure of the whole grain showing little dispersion; (a_{iv}) orientation change along a profile from mantle to core highlighted as a red arrow in (a_i); (b_i) CL image with 3D representation of crystal orientation and map of relative orientation change map with core marked; note oscillatory zoning coincides both with slight orientation changes and low index facets of crystal; (b_{ii}) low angle axis orientation in crystal coordinates for core and mantle; note axes are well defined for the core, while mantle shows different less well defined axes; (a_{iii}) Pole figure of the whole grain showing little dispersion; (b_{iv}) orientation change along a profile from mantle to core highlighted as a red arrow in (b_{ii});

Fig. 9: Crystallographic orientation relationships of zircon grains in the ferrodiorite dyke BG-1B; (a) Zrn 1Bb.3, (b) Zrn 1Bb.4, (c) Zrn 1Ba.5; (a_i) CL image with 3D representation of crystal orientation, (a_{ii}) relative orientation change map with mantle boundary marked; note part of the grain has a shape dictated by crystallography; (a_{iii}) pole figure of whole grain showing significant dispersion (top) and of area marked as a yellow box in (a_{ii}) (bottom), (a_{iv}) low angle misorientation axis in crystal coordinates of area marked as a yellow box (left) and whole grain; (a_v) orientation change along two profiles highlighted as black and red arrow in (a_{ii}); note the gradual increase as well subgrain (marked as blue arrow); (b_i) CL image with 3D representation of crystal orientation, (b_{ii}) relative orientation change map with core marked; note the coincidence of CL signature and orientation changes as well as the fact that in the mantle subgrain boundaries from core are continued perpendicular to the surface (white arrows); (b_{iii}) Pole figure of the whole grain showing clear

dispersion highlight by black arrow (top) and systematic dispersion of area marked in (b_{ii}); (b_{iv}) low angle misorientation axis in crystal coordinates for core and mantle; note axes are well defined for the core, while mantle shows different and less well defined axes; (b_v) orientation change along a profile highlighted as a black arrow in (b_{ii}); (b_{vi}) low angle misorientation axis in crystal coordinates for selected area marked as a yellow box in (b_{ii}); (c_i) CL image with 3D representation of crystal orientation, (c_{ii}) relative orientation change map with core marked; white round areas are due to LA-ICMPS spots for which no EBSD data could be obtained; (c_{iii}) pole figure of the whole grain showing some dispersion.

Fig. 10: (a) Ti-in-zircon temperature obtained using the formulations of Watson et al (2006) and Ferry and Watson (2007) in oscillatory zoned cores and chemically homogeneous mantles in zircon in BZGs (BG-5 and BG-7), and in the cauliflower-shaped zircons in ferrodiorite dyke (BG-1B). Note temperatures obtained using the formulation Ferry and Watson (2007) were computed a(TiO_2) = 0.7 and 0.9 in the absence of rutile, and the presence of ilmenite in the BZGs and ferrodiorite dyke. (b) The Ti-in-zircon temperatures are compared with metamorphic P-T values obtained from garnet-orthopyroxene/clinopyroxene-plagioclase-quartz assemblages in the Balangir anorthosite, border zone granitoids and ferrodiorites (Mukherjee et al., 1986; Nasipuri et al., 2011; Bhattacharya et al., 2021).

Fig. 11: CL images of representative zircon grains showing with U-Pb spot dates with 2σ errors (in Ma), and Wetherill diagrams showing discordia for (a) the BZGs (BG-5, 6 and 7), and (b) the ferrodiorite dyke (BG-1B). Data in Supplementary Material.

Fig. 12: (a) Wetherill concordia diagram showing the isotope values in cores and mantles in zircons in all rocks taken together (data in Supplementary Material). **(b)** CL images of representative zircon grains sequestered within coronal garnet showing ^{238}U-^{206}Pb spot dates with 2σ errors (in Ma), and the corresponding Wetherill concordia diagram. Data in the Supplementary Material.

Fig. 13: Schematic diagram showing in two stages the tectono-magmatic evolution of the study area (a, c) and the development of zircon characteristics at ~495 Ma (b, d); see text for details.

Supplementary Material [1]

LA-ICPMS analytical conditions, and analytical data and spot dates in zircon in three BZGs (BG-4, 5 and 7) and the ferrodiorite dyke BG-1B, Balangir anorthosite complex, Eastern Ghats Belt.

Supplementary Material [2]

Data for α-dosage calculations after Murakami et al. (1991) for understanding metamictization potential of zircons in this study.

Declaration of interests

☒The authors declare that they have no known competing financial interests or personal relationships that could have appeared to influence the work reported in this paper.

☐The authors declare the following financial interests/personal relationships which may be considered as potential competing interests:

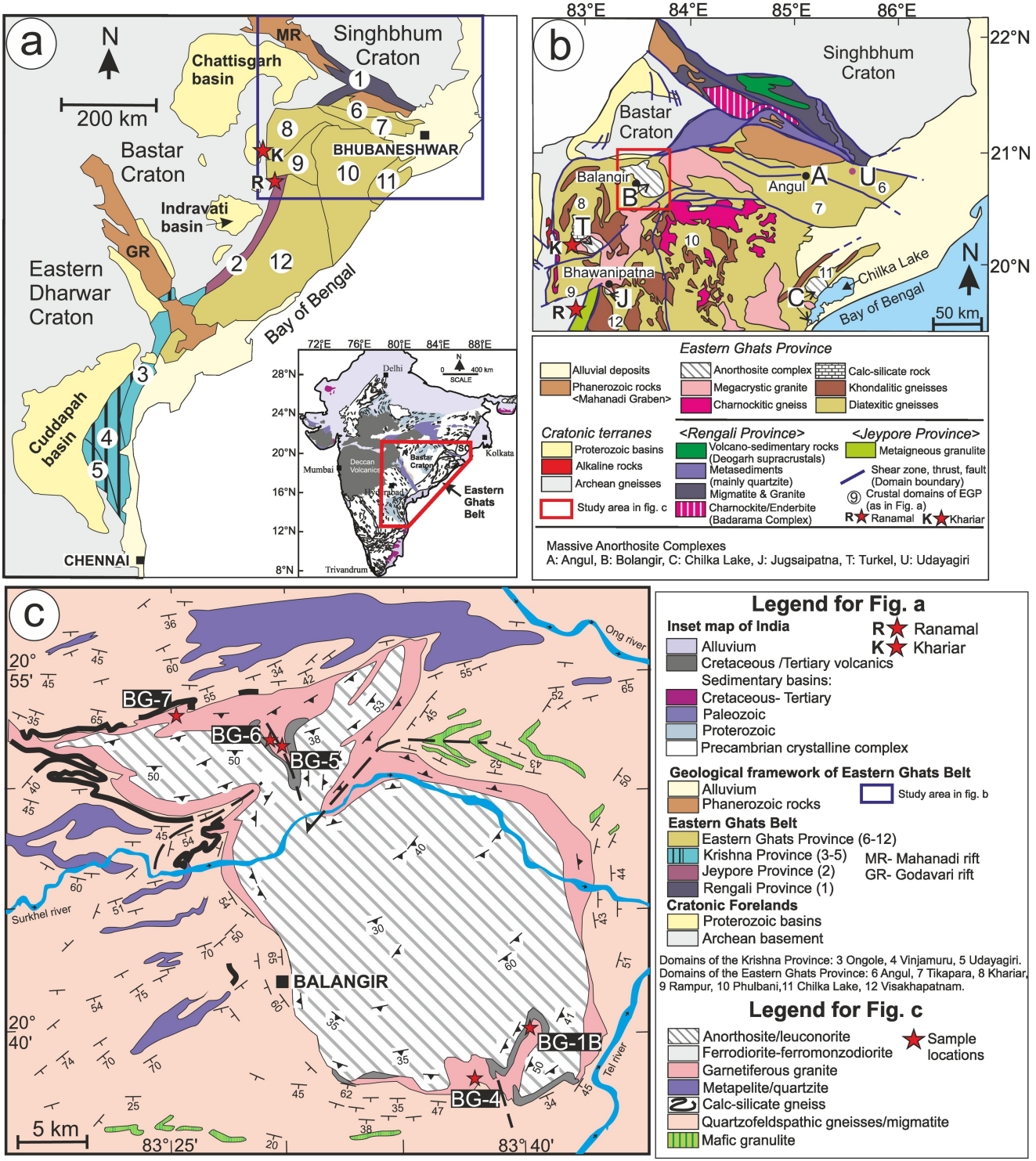
a
N
200 km
Chattisgarh basin
MR
Singhbhum Craton
1
6
7
8
K
9
10
11
BHUBANESHWAR
R
Bastar Craton
Indravati basin
GR
2
12
Eastern Dharwar Craton
Bay of Bengal
3
Cuddapah basin
4
5
CHENNAI
72°E
76°E
80°E
84°E
88°E
28°N
24°N
20°N
16°N
12°N
8°N
Delhi
Mumbai
Deccan Volcanics
Bastar Craton
Kolkata
Hyderabad
Trivandrum
Eastern Ghats Belt
0 400 km
SCALE
b
83°E
84°E
85°E
86°E
22°N
21°N
20°N
Singhbhum Craton
Bastar Craton
Balangir
B
Angul
A
U
6
7
8
T
K
10
Bhawanipatna
9
R
J
12
11
C
Chilka Lake
Bay of Bengal
N
50 km
Eastern Ghats Province
Alluvial deposits
Phanerozoic rocks <Mahanadi Graben>
Anorthosite complex
Megacrystic granite
Charnockitic gneiss
Calc-silicate rock
Khondalitic gneisses
Diatexitic gneisses
Cratonic terranes
Proterozoic basins
Alkaline rocks
Archean gneisses
Study area in fig. c
<Rengali Province>
Volcano-sedimentary rocks (Deogarh supracrustals)
Metasediments (mainly quartzite)
Migmatite & Granite
Charnockite/Enderbite (Badarama Complex)
<Jeypore Province>
Metaigneous granulite
Shear zone, thrust, fault (Domain boundary)
⑨ Crustal domains of EGP (as in Fig. a)
R Ranamal
K Khariar
Massive Anorthosite Complexes
A: Angul, B: Bolangir, C: Chilka Lake, J: Jugsaipatna, T: Turkel, U: Udayagiri
c
20° 55'
BG-7
BG-6
BG-5
Ong river
Surkhel river
BALANGIR
20° 40'
BG-1B
BG-4
Tel river
5 km
83°25'
83°40'
Legend for Fig. a
Inset map of India
R Ranamal
K Khariar
Alluvium
Cretaceous /Tertiary volcanics
Sedimentary basins:
Cretaceous- Tertiary
Paleozoic
Proterozoic
Precambrian crystalline complex
Geological framework of Eastern Ghats Belt
Alluvium
Phanerozoic rocks
Study area in fig. b
Eastern Ghats Belt
Eastern Ghats Province (6-12)
Krishna Province (3-5)
Jeypore Province (2)
Rengali Province (1)
MR- Mahanadi rift
GR- Godavari rift
Cratonic Forelands
Proterozoic basins
Archean basement
Domains of the Krishna Province: 3 Ongole, 4 Vinjamuru, 5 Udayagiri.
Domains of the Eastern Ghats Province: 6 Angul, 7 Tikapara, 8 Khariar, 9 Rampur, 10 Phulbani,11 Chilka Lake, 12 Visakhapatnam.
Legend for Fig. c
Anorthosite/leuconorite
Ferrodiorite-ferromonzodiorite
Garnetiferous granite
Metapelite/quartzite
Calc-silicate gneiss
Quartzofeldspathic gneisses/migmatite
Mafic granulite
Sample locations

Figure 1

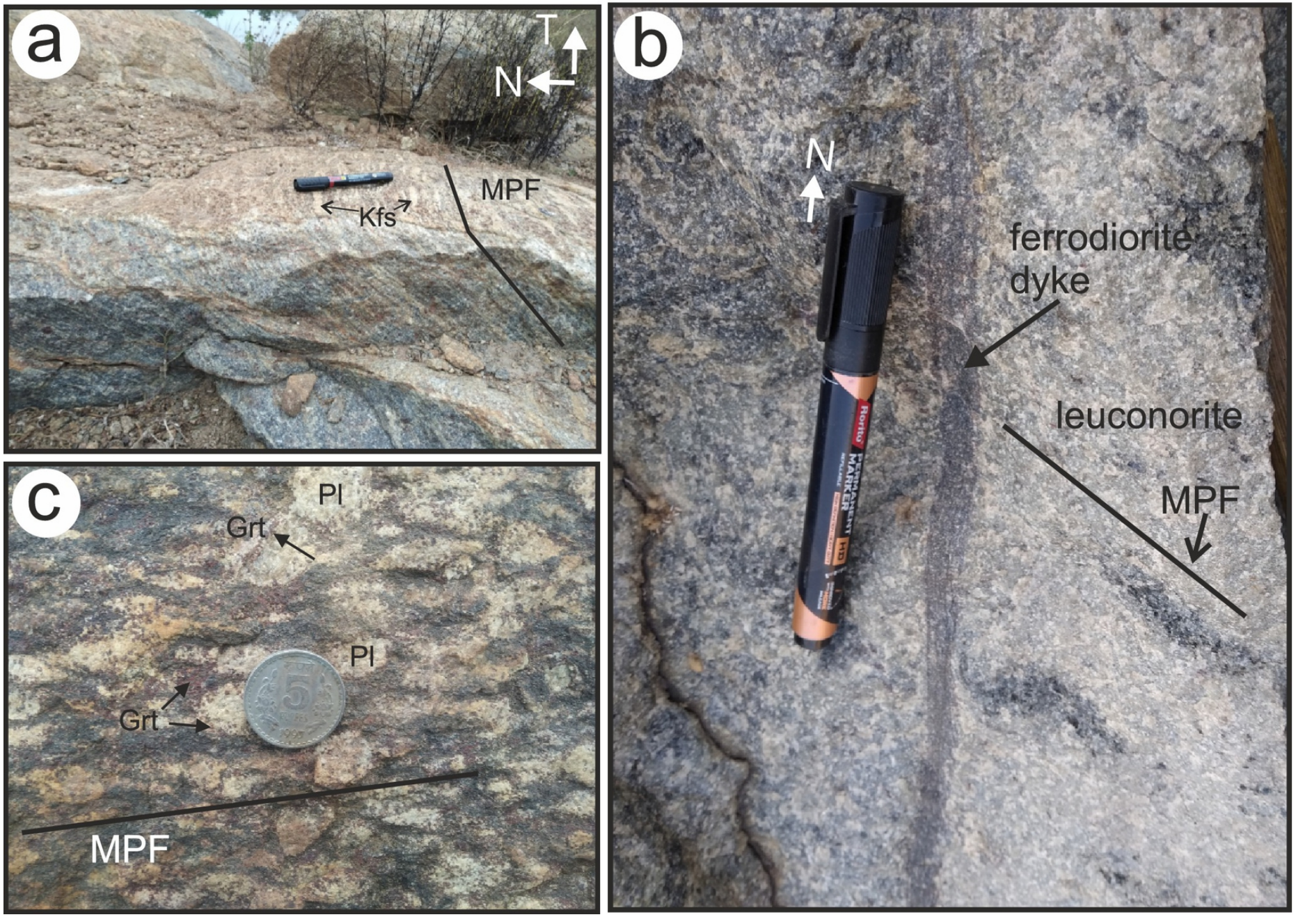
a
T
N
Kfs
MPF
b
N
ferrodiorite
dyke
leuconorite
MPF
c
Pl
Grt
Pl
Grt
MPF

Figure 2

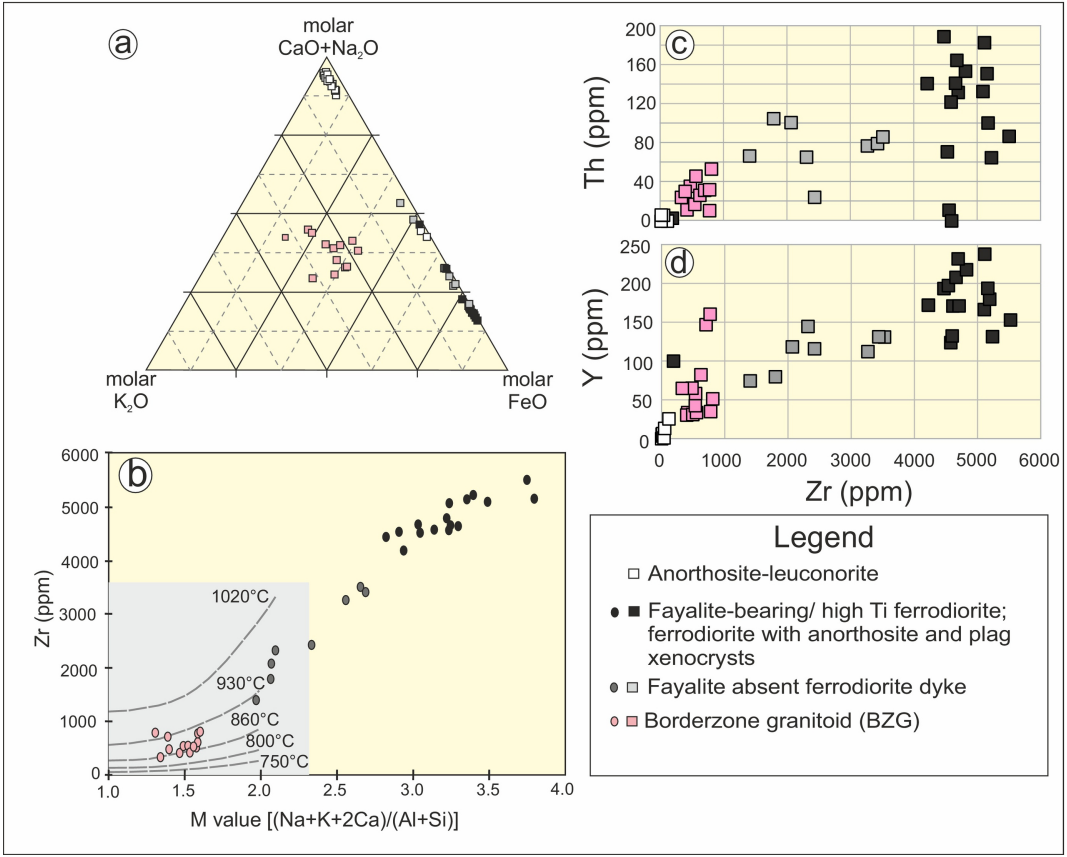
a
molar
CaO+Na2O
molar
K2O
molar
FeO
b
Zr (ppm)
M value [(Na+K+2Ca)/(Al+Si)]
1020°C
930°C
860°C
800°C
750°C
c
Th (ppm)
d
Y (ppm)
Zr (ppm)
Legend
Anorthosite-leuconorite
Fayalite-bearing/ high Ti ferrodiorite; ferrodiorite with anorthosite and plag xenocrysts
Fayalite absent ferrodiorite dyke
Borderzone granitoid (BZG)

Figure 3

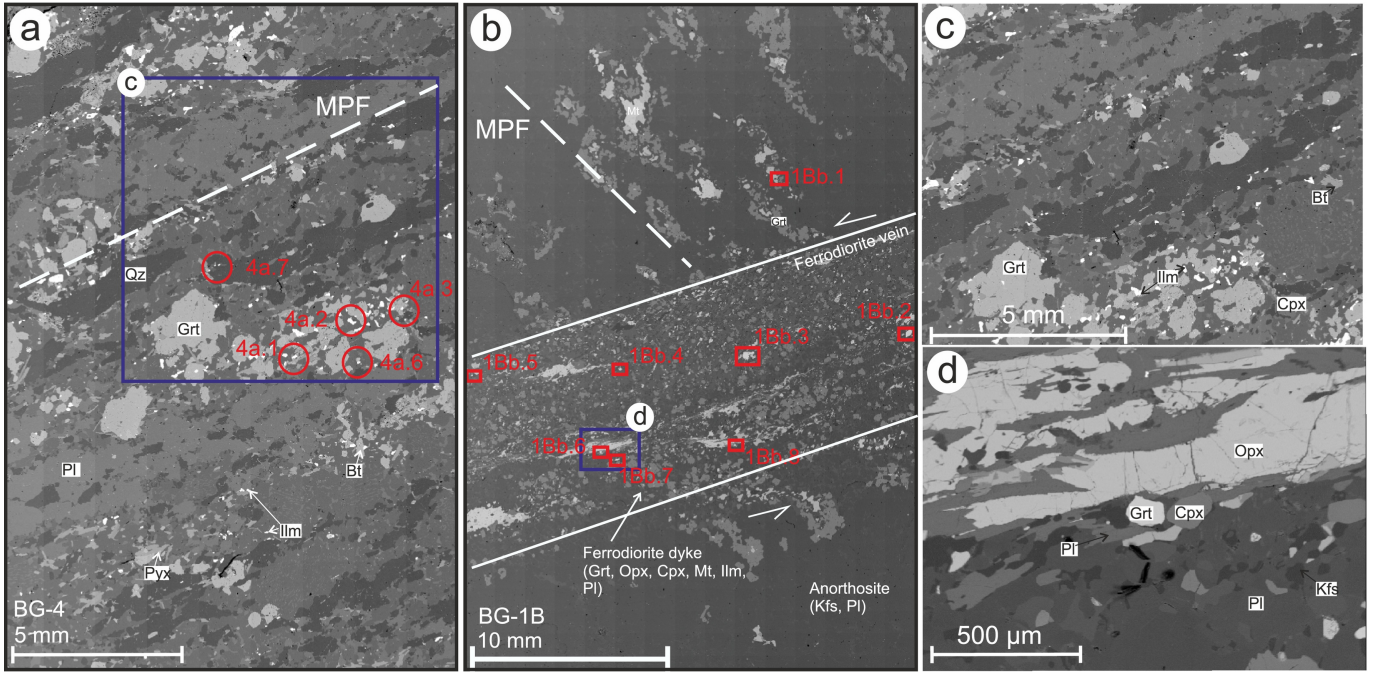
a
c
MPF
Qz
Grt
4a.7
4a.3
4a.2
4a.1
4a.6
Pl
Bt
Ilm
Pyx
BG-4
5 mm
b
MPF
1Bb.1
Grt
Ferrodiorite vein
1Bb.2
1Bb.3
1Bb.4
1Bb.5
d
1Bb.6
1Bb.7
1Bb.8
Ferrodiorite dyke
(Grt, Opx, Cpx, Mt, Ilm, Pl)
Anorthosite
(Kfs, Pl)
BG-1B
10 mm
c
Bt
Grt
Ilm
Cpx
5 mm
d
Opx
Grt
Cpx
Pl
Kfs
Pl
500 µm

Figure 4

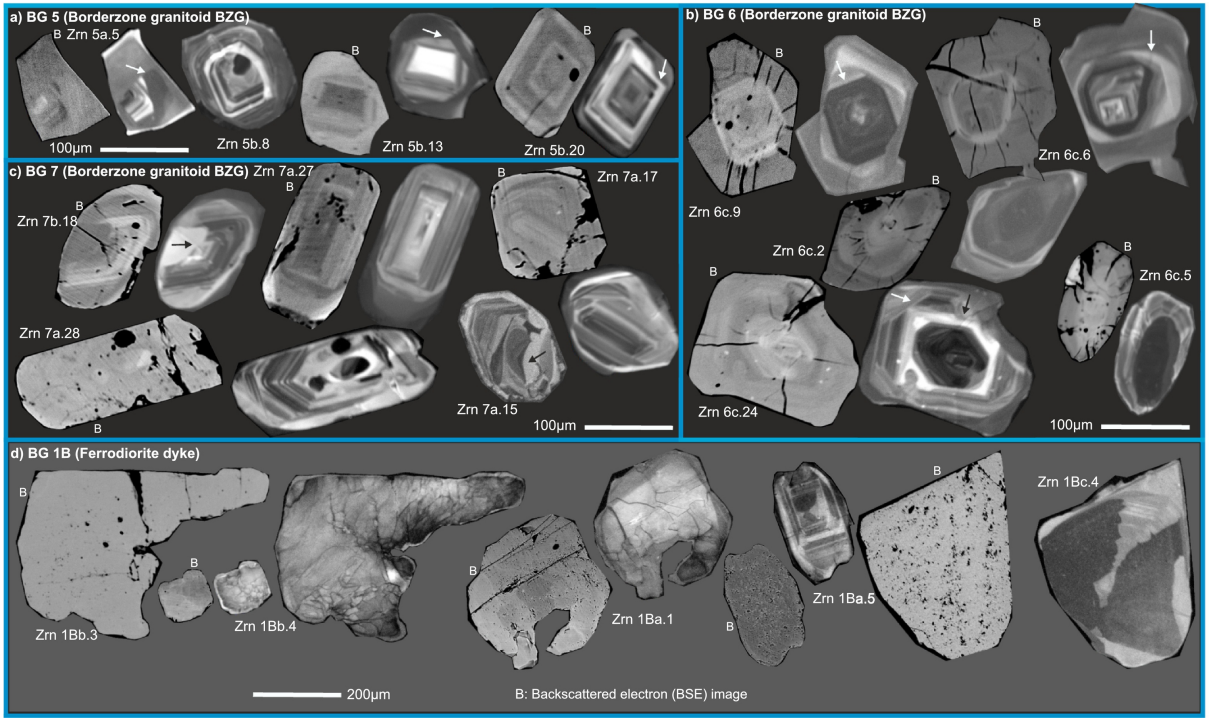
a) BG 5 (Borderzone granitoid BZG)
B Zrn 5a.5
Zrn 5b.8
Zrn 5b.13
Zrn 5b.20
100µm
b) BG 6 (Borderzone granitoid BZG)
Zrn 6c.6
Zrn 6c.9
Zrn 6c.2
Zrn 6c.5
Zrn 6c.24
100µm
c) BG 7 (Borderzone granitoid BZG)
Zrn 7a.27
Zrn 7a.17
Zrn 7b.18
Zrn 7a.28
Zrn 7a.15
100µm
d) BG 1B (Ferrodiorite dyke)
Zrn 1Bb.3
Zrn 1Bb.4
Zrn 1Ba.1
Zrn 1Ba.5
Zrn 1Bc.4
200µm
B: Backscattered electron (BSE) image

Figure 5

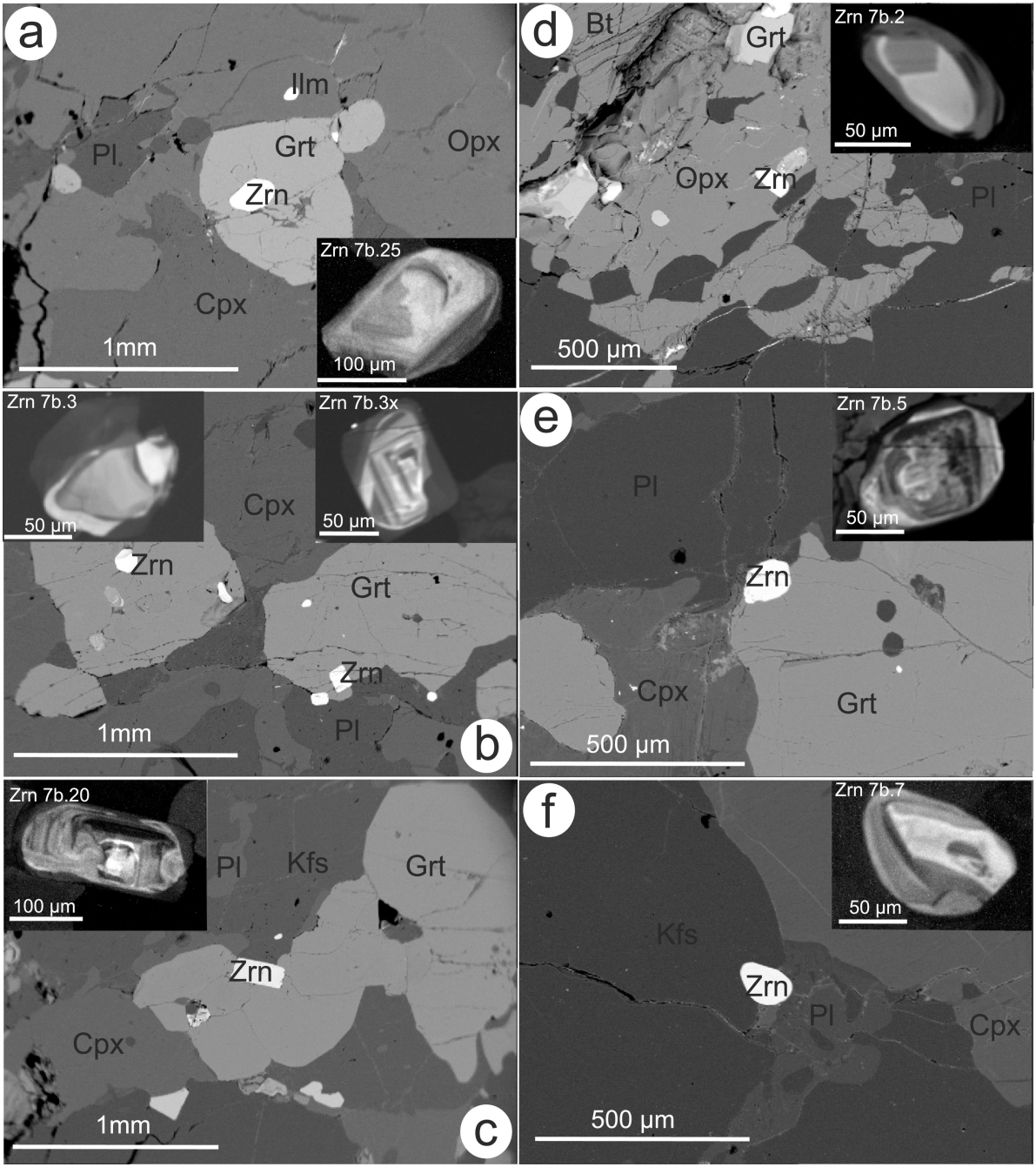
a
Ilm
Pl
Grt
Opx
Zrn
Zrn 7b.25
Cpx
1mm
100 µm
d
Bt
Grt
Zrn 7b.2
50 µm
Opx
Zrn
Pl
500 µm
Zrn 7b.3
50 µm
Zrn 7b.3x
50 µm
Cpx
Zrn
Grt
Zrn
1mm
Pl
b
e
Zrn 7b.5
50 µm
Pl
Zrn
Cpx
Grt
500 µm
Zrn 7b.20
100 µm
Pl
Kfs
Grt
Zrn
Cpx
1mm
c
f
Zrn 7b.7
50 µm
Kfs
Zrn
Pl
Cpx
500 µm

Figure 6

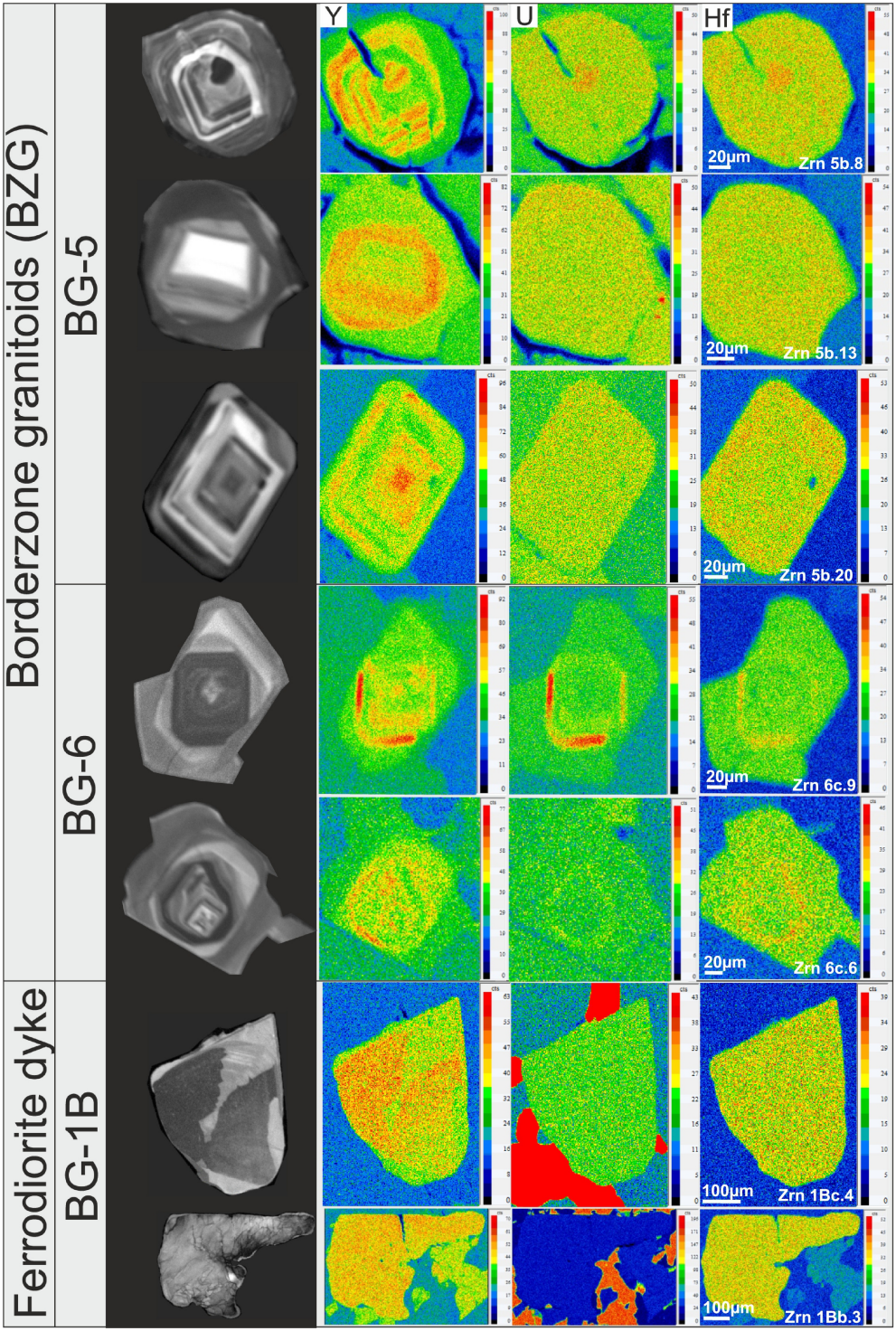
Borderzone granitoids (BZG)
BG-5
BG-6
Ferrodiorite dyke
BG-1B
Y
U
Hf
20µm
Zrn 5b.8
20µm
Zrn 5b.13
20µm
Zrn 5b.20
20µm
Zrn 6c.9
20µm
Zrn 6c.6
100µm
Zrn 1Bc.4
100µm
Zrn 1Bb.3

Figure 7

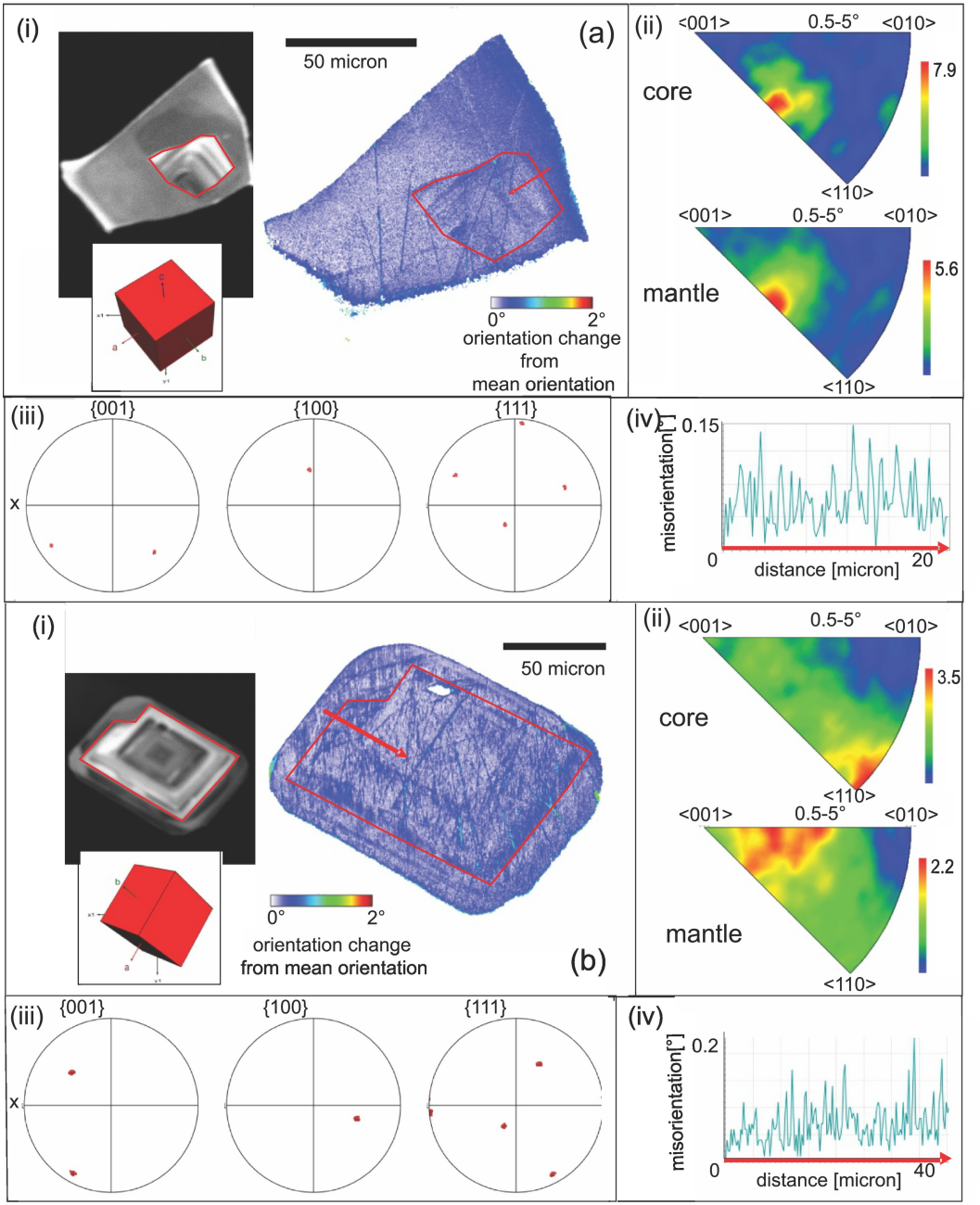
(i)
50 micron
(a)
0°
2°
orientation change
from
mean orientation
(ii)
<001>
0.5-5°
<010>
core
7.9
<110>
<001>
0.5-5°
<010>
mantle
5.6
<110>
(iii)
{001}
{100}
{111}
x
(iv)
misorientation[°]
0.15
0
distance [micron]
20
(i)
50 micron
0°
2°
orientation change
from mean orientation
(b)
(ii)
<001>
0.5-5°
<010>
core
3.5
<110>
<001>
0.5-5°
<010>
mantle
2.2
<110>
(iii)
{001}
{100}
{111}
x
(iv)
misorientation[°]
0.2
0
distance [micron]
40

Figure 8

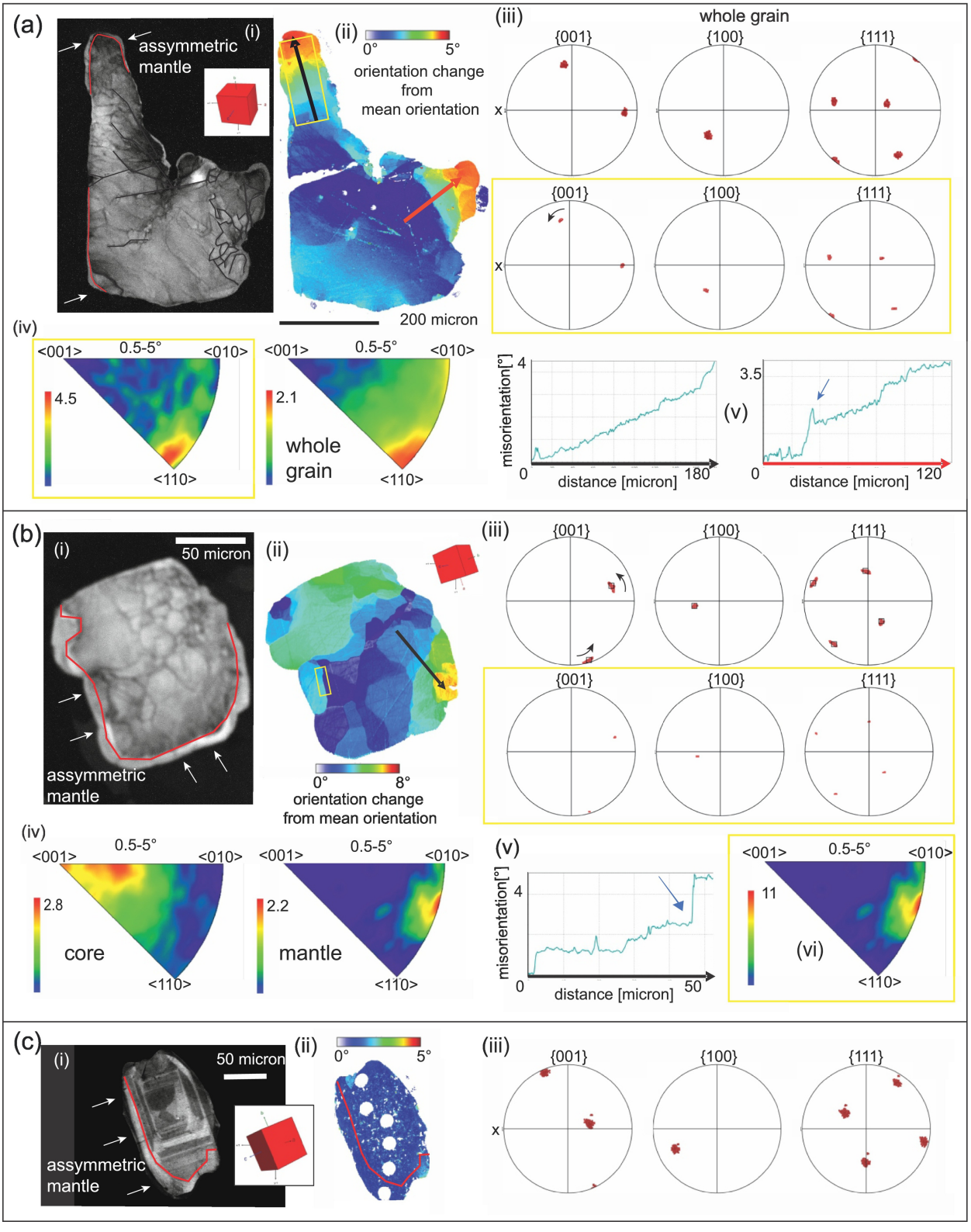
(a)
(i)
assymmetric mantle
(ii)
0°
5°
orientation change from mean orientation
200 micron
(iii)
whole grain
{001}
{100}
{111}
x
(iv)
<001>
0.5-5°
<010>
4.5
<110>
2.1
whole grain
misorientation[°]
4
0
distance [micron]
180
(v)
3.5
120
(b)
(i)
50 micron
assymmetric mantle
(ii)
0°
8°
orientation change from mean orientation
(iii)
(iv)
2.8
core
2.2
mantle
(v)
50
(vi)
11
(c)
(i)
50 micron
assymmetric mantle
(ii)
0°
5°
(iii)

Figure 9

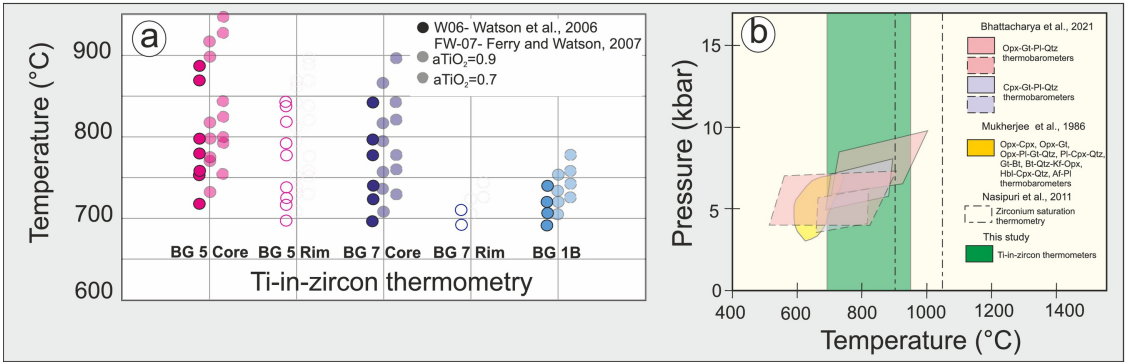
a
W06- Watson et al., 2006
FW-07- Ferry and Watson, 2007
aTiO2=0.9
aTiO2=0.7
Temperature (°C)
900
800
700
600
BG 5 Core
BG 5 Rim
BG 7 Core
BG 7 Rim
BG 1B
Ti-in-zircon thermometry
b
Bhattacharya et al., 2021
Opx-Gt-Pl-Qtz thermobarometers
Cpx-Gt-Pl-Qtz thermobarometers
Mukherjee et al., 1986
Opx-Cpx, Opx-Gt, Opx-Pl-Gt-Qtz, Pl-Cpx-Qtz, Gt-Bt, Bt-Qtz-Kf-Opx, Hbl-Cpx-Qtz, Af-Pl thermobarometers
Nasipuri et al., 2011
Zirconium saturation thermometry
This study
Ti-in-zircon thermometers
Pressure (kbar)
15
10
5
0
400
600
800
1000
1200
1400
Temperature (°C)

Figure 10

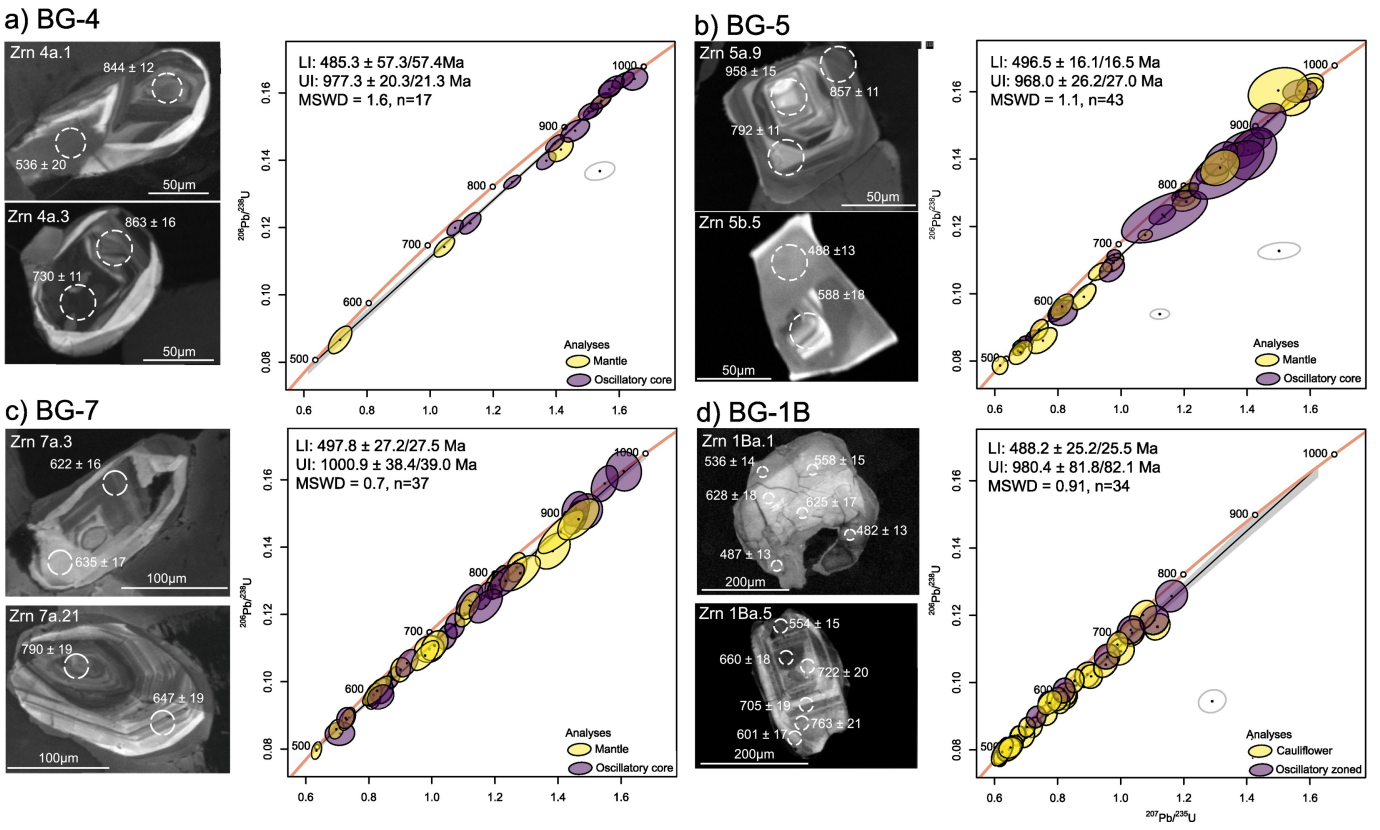
a) BG-4
Zrn 4a.1
844 ± 12
536 ± 20
50µm
Zrn 4a.3
863 ± 16
730 ± 11
50µm
LI: 485.3 ± 57.3/57.4Ma
UI: 977.3 ± 20.3/21.3 Ma
MSWD = 1.6, n=17
Analyses
Mantle
Oscillatory core
b) BG-5
Zrn 5a.9
958 ± 15
857 ± 11
792 ± 11
50µm
Zrn 5b.5
488 ±13
588 ±18
50µm
LI: 496.5 ± 16.1/16.5 Ma
UI: 968.0 ± 26.2/27.0 Ma
MSWD = 1.1, n=43
Analyses
Mantle
Oscillatory core
c) BG-7
Zrn 7a.3
622 ± 16
635 ± 17
100µm
Zrn 7a.21
790 ± 19
647 ± 19
100µm
LI: 497.8 ± 27.2/27.5 Ma
UI: 1000.9 ± 38.4/39.0 Ma
MSWD = 0.7, n=37
Analyses
Mantle
Oscillatory core
d) BG-1B
Zrn 1Ba.1
536 ± 14
558 ± 15
628 ± 18
625 ± 17
482 ± 13
487 ± 13
200µm
Zrn 1Ba.5
554 ± 15
660 ± 18
722 ± 20
705 ± 19
763 ± 21
601 ± 17
200µm
LI: 488.2 ± 25.2/25.5 Ma
UI: 980.4 ± 81.8/82.1 Ma
MSWD = 0.91, n=34
Analyses
Cauliflower
Oscillatory zoned
$^{206}Pb/^{238}U$
$^{207}Pb/^{235}U$

Figure 11

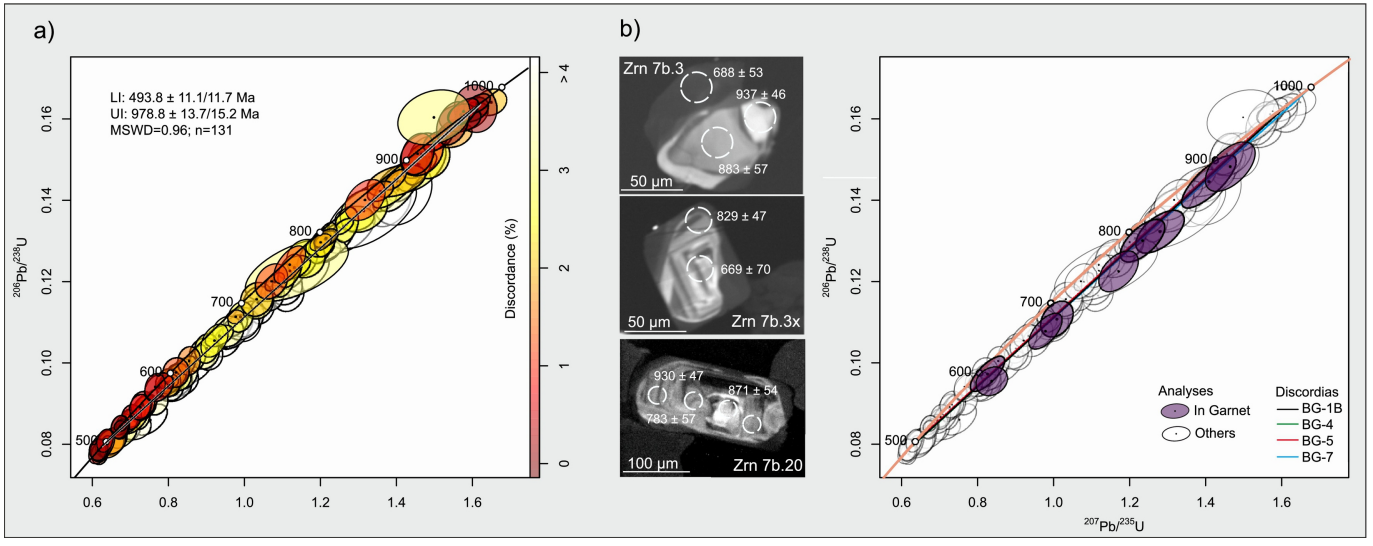
a)
LI: 493.8 ± 11.1/11.7 Ma
UI: 978.8 ± 13.7/15.2 Ma
MSWD=0.96; n=131
Discordance (%)
$^{206}Pb/^{238}U$
$^{207}Pb/^{235}U$
b)
Zrn 7b.3
688 ± 53
937 ± 46
883 ± 57
50 µm
829 ± 47
669 ± 70
50 µm
Zrn 7b.3x
930 ± 47
871 ± 54
783 ± 57
100 µm
Zrn 7b.20
Analyses
In Garnet
Others
Discordias
BG-1B
BG-4
BG-5
BG-7

Figure 12

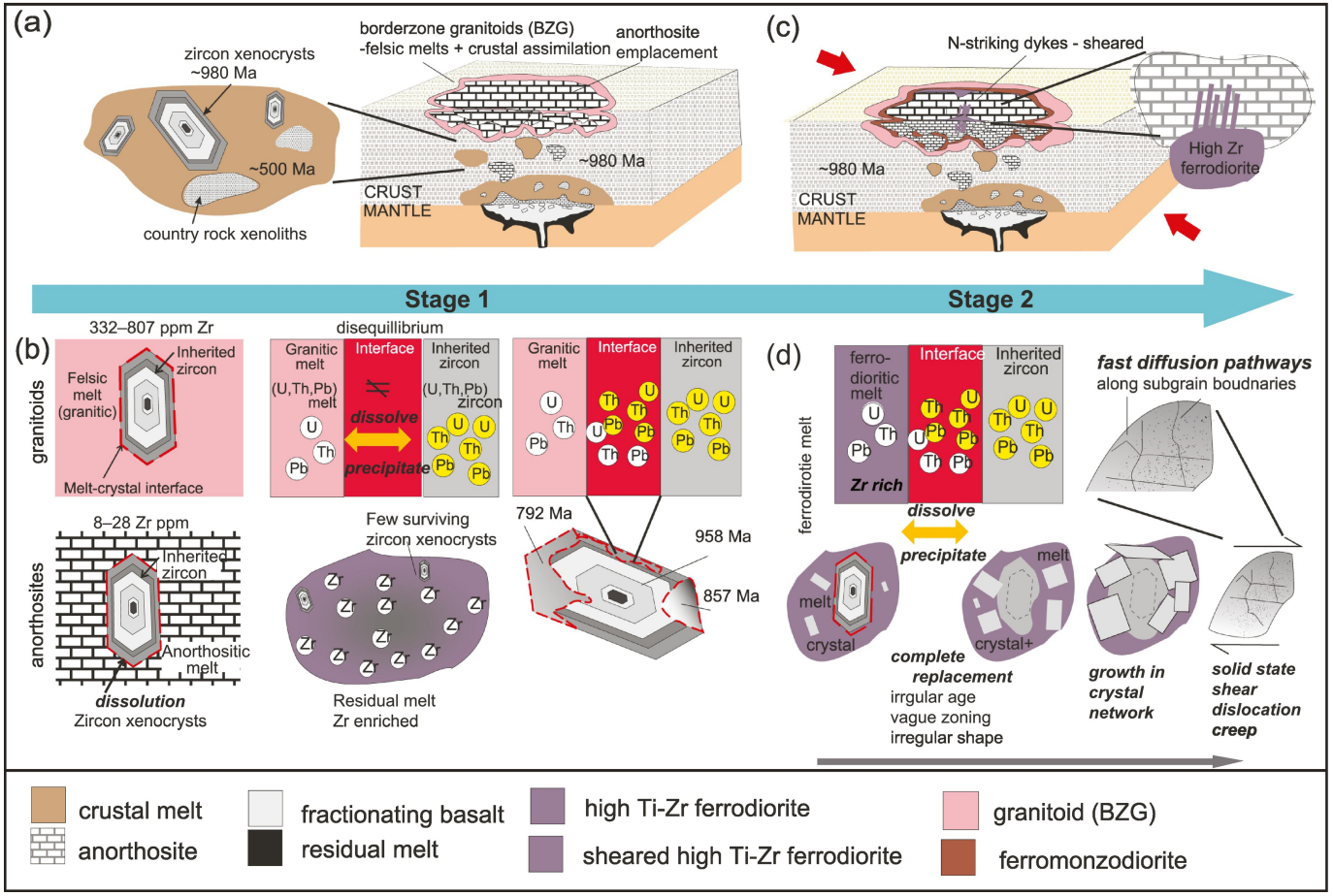
(a)
zircon xenocrysts
~980 Ma
~500 Ma
country rock xenoliths
borderzone granitoids (BZG)
-felsic melts + crustal assimilation
anorthosite
emplacement
~980 Ma
CRUST
MANTLE
(c)
N-striking dykes - sheared
~980 Ma
High Zr
ferrodiorite
CRUST
MANTLE
Stage 1
Stage 2
(b)
332–807 ppm Zr
granitoids
Felsic
melt
(granitic)
Inherited
zircon
Melt-crystal interface
8–28 Zr ppm
anorthosites
Inherited
zircon
Anorthositic
melt
dissolution
Zircon xenocrysts
disequillibrium
Granitic
melt
Interface
Inherited
zircon
(U,Th,Pb)
melt
(U,Th,Pb)
zircon
dissolve
precipitate
Few surviving
zircon xenocrysts
Residual melt
Zr enriched
Granitic
melt
Interface
Inherited
zircon
792 Ma
958 Ma
857 Ma
(d)
ferrodirotie melt
ferro-
dioritic
melt
Interface
Inherited
zircon
Zr rich
dissolve
precipitate
melt
crystal
crystal+
complete
replacement
irrgular age
vague zoning
irregular shape
fast diffusion pathways
along subgrain boudnaries
growth in
crystal
network
solid state
shear
dislocation
creep
crustal melt
anorthosite
fractionating basalt
residual melt
high Ti-Zr ferrodiorite
sheared high Ti-Zr ferrodiorite
granitoid (BZG)
ferromonzodiorite

Figure 13